Highly optimized embedded-atom-method potentials for fourteen fcc metals

H. W. Sheng, M. J. Kramer, A. Cadien, T. Fujita, and M. W. Chen

Phys. Rev. B **83**, 134118 — Published 20 April 2011

DOI: 10.1103/PhysRevB.83.134118

Highly Optimized Embedded-Atom-Method Potentials for 14 fcc Metals

H.W. Sheng[1], M.J. Kramer[2], A. Cadien[1], T. Fujita[3], M.W. Chen[3]

[1]*School of Physics, Astronomy and Computational Sciences, George Mason University, Fairfax, VA 22030, USA*

[2]*Materials Science and Engineering, Ames Laboratory (USDOE), Ames, Iowa 50011, USA*

[3]*WPI Advanced Institute for Materials Research, Tohoku University, Sendai 980-8577, Japan*

Abstract

Highly optimized embedded-atom-method (EAM) potentials have been developed for 14 face-centered cubic (fcc) elements across the periodic table. The potentials were developed by fitting the potential energy surface (PES) of each element derived from high-precision first-principle calculations. The as-derived potential energy surfaces were shifted and scaled to match experimental reference data. In constructing the PES, a variety of properties of the elements were considered, including lattice dynamics, mechanical properties, thermal behavior, energetics of competing crystal structures, defects, deformation paths, liquid structures, and so forth. For each element, the constructed EAM potentials were tested against the experiment data pertaining to thermal expansion, melting, and liquid dynamics via molecular dynamics (MD) computer simulation. The as-developed potentials demonstrate high fidelity and robustness. Owing to their improved accuracy and wide applicability, the potentials are suitable for high-quality atomistic computer simulation of practical applications.

I. Introduction

The thermodynamics and kinetics of materials are dictated by their potential energy surfaces (PES), [1] which can be seen as a function of atomic positions. Hence, to investigate material behavior under various thermodynamic conditions, proper descriptions of the interactions between atoms are necessary. Quantum mechanics provides the basis for accurate derivation of the total energy of any given system,[2,3] but unfortunately, at the current time, approaches based on quantum mechanics are still limited to small systems, which renders them intractable for large-scale computer simulation,[4] especially for metals. Therefore, for large-scale computer simulation (both spatially and temporally), computationally less intensive approaches toward atomic interactions, without compromising too much of the accuracy of quantum mechanics, are routinely in demand. To that end, the objective of this paper is to develop high-quality, semi-empirical interatomic potentials for fcc elements.

For metals, a widely used semi-empirical potential formalism is the embedded-atom method (EAM), [5-8] which is rooted in the density functional theory (DFT).[9] Over the last twenty years, a number of other many-body potential models have been proposed, many of which also originated from quantum mechanics and share similar mathematical forms with the EAM , such as the Finish-Sinclair model,[10-12] second-order moment approximation of tight-binding,[13] and the effective-medium-theory model,[14,15] to name a few. The EAM potential model overcomes several problems encountered with two-body potentials, for instance, the coordination independence of bond-strength and the zero value for the Cauchy pressure for metals ($C_{12} - C_{44} = 0$). Currently, EAM potentials have been applied to study many aspects of materials behavior, mostly semi-quantitatively.

The popularity of the EAM model (and similar models) results from its underpinnings in quantum mechanics, as well as its mathematic simplicity, which makes it conducive to large-scale computer modeling. Parameterization of different EAM models aimed at developing new EAM potentials with better accuracy and applicability has been a recurring theme in literature. A recent popular practice for developing interatomic potentials is to fit the PES of small systems derived by first-principles calculations, [16, 17]

with or without experimental data; the well-known "force-matching" method, originally proposed by Ercolessi and Adams [18] belongs in this category. In the force-matching method, the forces of each atom calculated from semi-empirical potentials are optimized to match first-principles data (i.e., the slopes of the PES). So far, the PES-fitting method has been used to construct potentials for various materials such as metallic elements, alloys, semiconductors, and molecules.[16-22] However, due to the tedious nature of this fitting process, the number of interatomic potentials derived from PES-fitting is still limited in literature.

While a plethora of EAM potentials have been developed for metals over the decades, especially for pure elements, most of them were fitted to a limited number of experimental data, and may not be adequate to describe phase spaces where the potentials were not "trained", thus exhibiting inevitable shortcomings. In this work, we were motivated to develop EAM potentials with better overall performances (i.e., improved accuracy and wider applicability) by using the PES-fitting method. Different from previous models, we laid special emphases on lattice dynamics as well as liquid structures and dynamics, which have not received enough attention in previous works. In this paper, details of the fitting procedure and their results will be presented using Au as an example. Au was chosen for the following two reasons: firstly, among the late transition metals, Au is believed to be difficult for high-level EAM parameterization. [24-26] Secondly, there already exists in literature several many-body potentials developed for Au over the years,[6,23-27] which in turn can be exploited here to evaluate the accuracy or deficiency of the current potential model. Such potential fitting efforts have been extended systematically to 14 fcc metals across the periodic table, including 8 transition metals (Ni, Cu, Rh, Pd, Ag, Ir, Pt, Au), two simple metals (Al, Pb), two alkaline earth metals (Ca, Sr) and two rare earth metals (Ce, Yb). For all the elements studied, key fitting results will be tabulated and compared with experimental data whenever available. The EAM potentials developed for these metals have been made available through the World Wide Web[28] with formats compatible to several atomistic simulation packages, such as LAMPS,[29] IMD,[30] DL_POLY,[31] and XMD.[32]

II. Computational Methodology

A. Selection of atomic configurations

To obtain the PES of each element, a few hundred atomic configurations were selected and subjected to high-precision DFT calculations (see below), with each configuration typically containing approximately 100 atoms. The DFT data were then used to represent the PES of each element for potential fitting described in section II.C. The selected configurations span a wide range of the phase space and encompass phases encountered in typical materials research. The atomic configurations can be categorized into the following groups:

(1) *Equations-of-state of different crystal structures*. In the present work, equations-of-state (EOS) of six crystal structures with distinct space-group numbers were considered: face-centered cubic (fcc), body-centered cubic (bcc), hexagonal close packing (hcp), 9R, simple cubic (sc), and diamond cubic (dc) structures. For each crystal structure, we calculated at least 12 atomic volumes spanning from $\sim 0.5V_0$ to $\sim 3.5V_0$ (V_0 stands for the equilibrium atomic volume of the element).

(2) *Defects in fcc crystals*. For each element, a large collection of crystal defects were included: point defects (vacancies, interstitials), planar defects (surfaces and stacking faults), and clusters (less than 25 atoms). The defects were relaxed using *ab initio* geometric optimization techniques.

(3) *Deformation paths.* Two archetypal deformation paths were studied: the fcc-bcc Bain deformation path and the trigonal Bain deformation path. Along each deformation path, more than 20 configurations were selected.

(4) *Trajectories along the melting process of fcc crystals.* Using NVT (constant number of particles, volume, and temperature) ensembles, *ab initio* MD simulations were performed to simulate the melting process of the fcc structure of each element at different number densities. To simulate melting, each *ab initio* MD run typically lasts 1200 steps with a 2 fs time-step. Along each melting trajectory, 10 configurations were selected at different temperatures, which are important in capturing the thermal behavior of crystals upon heating.

(5) *Equations-of-state of liquids at different temperatures.* Well-equilibrated liquids were compressed and dilated uniformly to different volumes at high temperatures. Ten configurations were selected to represent the EOS of the liquid, which are deemed essential to simulate the liquid dynamics of the elements.
(6) *Trajectories along the cooling process of liquids*. The liquids equilibrated at high temperatures were quenched at a fast rate to room temperature to obtain the glass structures employing *ab initio* MD. Ten configurations were obtained along each quench trajectory.
(7) *MD-important configurations.* Configurations along classical MD trajectories employing *ad hoc* EAM potentials were added to the *first-principles* database during subsequent iterative runs to improve the pre-existing EAM potentials. Classical MD was typically performed with NPT ensembles (constant number of particles, pressure and temperature) to simulate the melting process of each metal.

B. DFT calculation

Ab initio calculations were performed using the pseudopotential and planewave method implemented in the Vienna *Ab-initio* Simulation Package (VASP).[33] In all the VASP calculations, the projected augmented waves (PAW)[34] method and the generalized-gradient approximation (GGA) were used. The spin polarization effect was not considered in the current work. The PAW-based pseudopotentials were generated by Kress[35] and provided with the commercial VASP package. The valence electrons of each element during *ab initio* calculations are specified in Table I. For high-precision single-point electronic structure calculation, we typically used 3x3x3 Monkhorst-Pack k-point grids,[36] which ensure that the total energy is converged within 2~5 meV/atom. For *ab initio* molecular dynamics and geometry optimization, only the Γ point was used, which was found to be adequate for the large unit-cells involved.

C. Potential fitting procedure

The embedded atom method was used to fit the PES of the systems, which is written as:[4]

$$E_{tot} = \sum_{i,j} \phi(r_{ij}) + \sum_{i} F(n_i) \text{ and } n_i = \sum_{j} \rho(r_{ij}) \quad (1)$$

where $\phi(r)$, $\rho(r)$ and $F(n_i)$ are the pair, density, and embedded functions. For the meanings of the three functions, the reader is referred to Ref. [4]. Analog to this analytic form is the glue model. [15] Here, we express the three functions with quintic spline functions for each element. The choice of high-order spline functions (quartic or quintic splines) over cubic splines is to ensure smooth interpolations of the second derivatives of the total energy of the system. We opted for quintic splines because they are mathematically convenient to implement in computational codes. To this end, we adopted the algorithm proposed by Herriot and Reinsch[37] for natural quintic spline interpolations. We typically used 15 equidistant spline knots for both the density and the pair functions, and 6 spline knots for the embedding function. Both the density and pair functions, as well as their first and second derivatives with respect to r are forced to be 0 at a cutoff distance, which is set to be slightly larger than the fifth atomic shell in their equilibrium fcc lattices. Potentials with shorter cutoff distances have also been developed and are available upon request, but their results will not be discussed in the current paper. Since *ab initio* data are difficult to come by at very short interatomic distances, we limit our fitting range of the EAM potentials to a minimum distance of 1.5 Å. Smooth spline functions can be used to extrapolate the functions to smaller interatomic distances.

For PES potential fitting, the forces on the atoms, total energies, and stress tensors of all configurations obtained from first-principles calculations were gathered in the fitting database. However, due to several approximations, DFT calculations do not always generate results that match experimental data (e.g., DFT with GGA approximations often overestimates the lattice constants of transition metals). To eliminate the discrepancies between DFT calculations and experimental data, we set out to deform the PES using linear scaling. The following two transforms were applied to the PES:

$$\mathbf{R} \to A \cdot \mathbf{R} \text{ and } E \to B \cdot E + C, \quad (2)$$

where $\mathbf{R}$ and E are the atomic coordinates and potential energy of the system, and A, B, C are transformation parameters, determined based on the following rules: The PES was scaled and shifted such that the new PES described by EAM potentials yields the lattice constants and cohesive energy at room temperature, and the liquid density at the melting temperature to be consistent with experimental values. In other words, for the two transformations, A sets the length scale; B controls the liquid density; and C adjusts

the cohesive energy. The three transformation parameters were obtained through a recursive scheme with the following steps.

(1) Obtain A by matching the lattice constant using the pre-parameterized EAM potential, and transform the PES according to Eq. (2).
(2) Re-parameterize the EAM potential.
(3) Obtain B by matching the liquid density using the pre-parameterized EAM potential, and transform the PES according to Eq. (2).
(4) Re-parameterize the EAM potential.
(5) Obtain C by matching the cohesive energy using the pre-parameterized EAM potential, and transform the PES according to Eq. (2).
(6) Re-parameterize the EAM potential.
(7) Repeat step (1) until A, B and C converge.

While the energy shift C can be determined with relative ease, the determination of A and B needs more fine-tuning, as the two quantities are weakly coupled: the scaling of the coordinates will have an effect on the liquid density of the system, and vice versa. Through a few iterations, we found that in the best values A typically lies in the range of 0.975~1.015 and B lies in the range of 1.0 ~ 1.5, depending on the element (listed in Table I). Next, forces on all atoms and stress tensors of each configuration were rescaled accordingly. Although different in details, a similar practice was performed by Grochola et al., [26] in fitting an Au EAM potential. It is worth noting that the rescaling scheme presented here is only an empirical workaround to overcome accuracy issues encountered in DFT calculations. This way, the deformed first-principles PES has better agreement with the experiments. In the following sections, we refer to all *ab initio* data as the transformed data.

We further augmented the database by including other reliable experimental data, such as phonon frequencies and elastic constants, at different temperatures. We typically fit the phonon frequencies ν_i (both longitudinal and transverse modes) of equilibrium fcc structures at the X point, and three elastic constants (C_{11}, C_{12} and C_{44}) of equilibrium fcc

structures. Altogether, they comprise the fitting database for the potential development explained below.

The simulation package POTFIT[17], after non-trivial modifications (e.g., implementation of quintic spline interpolation, phonon and elastic constants calculation, and optimization techniques, etc), has been employed for potential fitting. Details of the POTFIT protocols can be found in Ref. [17]. In short, the potential fitting is essentially a nonlinear optimization process, with the fitting error defined through a least-squares function formed from the differences of the EAM and DFT (and experiment) values:

$$Z = Z_F + Z_S + Z_E + Z_P + Z_B, \tag{3}$$

where

$$Z_F = \sum_{i=1}^{N_A} \sum_{j=1}^{3} W_i \frac{(F_{i,x_j}^{EAM} - F_{i,x_i}^{DFT})}{(F_{i,x_j}^{DFT})^2 + \varepsilon_i},$$

$$Z_S = \sum_{i=1}^{N_c} \sum_{j=1}^{6} W_i \frac{(\sigma_{i,j}^{EAM} - \sigma_{i,j}^{DFT})^2}{(\sigma_{i,j}^{DFT})^2},$$

$$Z_E = \sum_{i=1}^{N_C} W_i \frac{(E_i^{EAM} - E_i^{DFT})^2}{(E_i^{DFT})^2},$$

$$Z_P = \sum_{i=1}^{N_p} W_i \frac{(\nu_i^{EAM} - \nu_i^{EXP})^2}{(\nu_i^{EXP})^2}$$

and

$$Z_B = \sum_{i=1}^{N_B} W_i \frac{(B_i^{EAM} - B_i^{EXP})^2}{(B_i^{EXP})^2}$$

are contributions from forces, stress tensors, total energies, phonons, and elastic constants, respectively. In the above definitions, W_i denotes the fitting weights of different components, N_A the number of atoms in the database, F_{i,x_j} the atomic force along the x_j direction, N_c the number of atomic configurations, $\sigma_{i,j}$ the j the component of the stress tensor, E_i the cohesive energy of ith atomic configuration, N_p the number of phonon frequencies, N_B the number of elastic constants, and ν_i and B represent phonon

frequency and elastic constant, respectively. The fitting weights, W_i, were introduced by an trial-and-error approach with special attention paid to the properties of defects. In fact, we also included an additional penalty function in the cost function Z of Eq. (3) to impose constraints on a few terms. Specifically, we wanted the density function to be everywhere positive, and the second derivative of the embedding function to be positive, i.e., $\rho(r) > 0$ and $F''(\rho) > 0$. In the present work, we adopted the simulated annealing technique [38] to minimize the target function Z, namely the difference between the transformed PES and the one evaluated from *ad hoc* EAM potentials. Optimized potentials were finally obtained once the target function showed no sign of decrease after prolonged simulation time.

III. Results and Discussion

In the present work, since a total of 36 fitting parameters were used in quintic spline interpolations to represent the three functions $\phi(r)$, $\rho(r)$ and $F(n_i)$ in the EAM formalism, which introduces flexibility in potential fitting, it is essential to examine the profiles of the three functions to show they are not ill-behaving, wavy curves. Fig. 1 shows the profiles of the three functions for Au, and demonstrates that the profiles are slowly varying, suggesting that the fitting results are not from non-physical mathematical entities.

To demonstrate the overall performance of the as-developed EAM potential, we first compare the present EAM model with previous models for Au in terms of the accuracy of predicting a set of materials properties, as shown in Table II. It can be seen that the present EAM potential is able to produce better matches with experiments, such as elastic constants, vacancy formation energy, stacking fault energy, melting temperature, liquid density and energy differences between fcc, hcp, and bcc structures, etc. In the following, we further analyze materials properties predicted by the as-developed EAM potentials. Through comparisons with DFT data (which were used in potential fitting), we demonstrate the applicability of the optimized EAM potentials.

A. Lattice dynamics

In this section we demonstrate that the optimized EAM potentials can adequately address the issue of lattice dynamics. All lattices have thermal vibrations at finite temperatures, and consequently, the equilibrium lattice parameters of the lattices change with temperature. At a given temperature, correct derivation of the equilibrium lattice parameter $a_e(T)$ should be preceded by minimizing the Helmholtz free energy $F(a,T)$ of the crystal at ambient pressure. Unfortunately, in a majority of previous EAM treatments, the temperature effect was explicitly neglected. The equilibrium lattice constants were often taken as the values corresponding to the minimum of the total energy $E_{tot}(a)$.

In computer simulations, there are several distinct approaches to treating the temperature effect, such as the quasi-harmonic approximation (QHA) [39,40] and the molecular dynamics (or Monte Carlo) method. [3] Both treatments are approximate methods complimentary in different temperature regimes. Atomic vibrations, in the limit of absolute zero temperature, are purely harmonic, and therefore, in the low temperature regime, one can use the quasi-harmonic approximation (QHA) to treat vibrating lattices and ignore the anharmonic lattice vibration effect. As temperature increases, phonon-phonon coupling becomes significant and even atomic diffusion becomes possible. In this temperature regime, one has to switch to alternative approaches, such as molecular dynamics (MD) or Monte Carlo (MC) to treat lattice dynamics. MD or MC methods, however, are not suitable for low-temperature lattice dynamics because the quantum effect (i.e., zero-point vibration[41]) is not considered in these two approaches.

In the present work, in order to obtain the equilibrium lattice parameter, we performed both the QHA and MD methods to evaluate the temperature effect of the systems. In the QHA, the total Helmholtz free energy of the crystal at temperature *T* and lattice constant *a* is given by:

$$F(a,T) = E_{tot}(a) + E_{ZPT}(a) + k_B \sum_{\mathbf{q},s} \ln\left\{2\sinh\frac{h\nu_s(\mathbf{q},a)}{2k_BT}\right\} \qquad (4)$$

where $E_{tot}(a)$ is the static energy given by Eq.(1) at a given volume V, or lattice constant *a*. $\nu_s(\mathbf{q},a)$ is the phonon frequency of *s*th mode for a given wave vector **q** and lattice constant *a*; k_B is the Boltzmann constant, and h Plank's constant. $E_{ZPT}(a)$ is the zero-

point energy defined as $E_{ZPT}(a) = \frac{1}{2}\sum_{\mathbf{q},s} h\nu_s(\mathbf{q},a)$.

Thus, the evaluation of the total Helmholtz free energy $F(a,T)$ in the QHA pertains to the assessment of the vibrational properties of the system. For any given lattice parameter and wave vector, the phonons can be computed by diagonalizing the dynamical matrix derived from the EAM potential according to:[41]

$$D_{\lambda\mu}(\mathbf{q}) = \sum_{\mathbf{R}} \frac{1}{\sqrt{m_i m_j}} \frac{\partial^2 E_{tot}}{\partial\alpha\partial\beta} \exp\left[i\mathbf{q}\cdot(\mathbf{r}_{ij}+\mathbf{R})\right] \quad (5)$$

where *i* and *j* are particle indices; m_i and m_j are masses of particle *i* and *j*; α and β are force components (*x*, *y*, or *z*); $\lambda = 3i+\alpha$ and $\mu = 3j+\beta$; $\mathbf{r}_{ij}$ is the displacement vector between particle *i* and *j*. The summation over **R** represents the sum over lattice vectors within the cutoff radius.

The phonon dispersion curves of Au are computed using the optimized EAM potential, as shown in Figure 2. The lattice parameter for phonon calculations of fcc Au in Fig. 2 is set to 4.078 Å, which corresponds to the experimental value at room temperature. Experimental measurements of the phonon dispersion curves at this temperature are provided (red symbols in Fig.2).[42] For comparison, *ab initio* phonon dispersion curves using the plane-wave self-consistent field (PWSCF) simulation package[43] are also shown. All branches of the phonon-dispersion curves evaluated from Eq. (5) are in reasonable agreement with the experiment, indicating that the EAM can adequately describe the lattice vibrations of Au at room temperature. The phonon dispersion curves for all other fcc metals have been evaluated using their optimized EAM potentials. Table IV lists selected phonon frequencies at the following k-points: X, L, and K; only the phonon frequencies at the X point were fitted. The overall agreement between experiment and EAM calculation is equally satisfactory, except for Pb where the electronic spin-orbit effect was found important but not considered in this work. The average discrepancy between experimental and calculated phonon frequencies at those special points is less than 5 percent.

Having established the validity of phonon calculation, in obtaining the wave vector sum in Eq. (4), we integrated over 85 pre-defined k-points in the irreducible Brillouin zone

(IBZ). The k-point vectors, as well as their weights, were adopted form the NRL tight-binding calculation package.[44] Temperature variation of thermodynamic properties is studied from 0 to 800 K in steps of 2 K. At each given temperature *T*, the equilibrium lattice parameter is obtained by minimizing $F(a,T)$, with respect to *a*. The variations of the lattice constant in the QHA are shown in Fig.3 as a function of temperature, with and without the zero-point energy E_{ZPT} included in $F(a,T)$. It is evident that the zero-point energy plays a role in determining the equilibrium lattice parameter. For example, at zero temperature, the lattice parameter changes from 4.061 Å to 4.066 Å after taking into account the zero point energy.

Employing the same EAM potential, MD simulation of fcc Au shows its thermal behavior upon heating up to the melting temperature. Compared with experimental observations, it is found that MD simulation predicts correct thermal expansion behavior of Au at temperatures higher than 250 K. By contrast, at low temperatures the QHA is more appropriate to describe the lattice dynamics of Au.

During potential fitting, the equilibrium lattice constants were evaluated using either the QHA or MD techniques, depending on the nature of the system. For transition metals, whose melting temperatures are normally high, we used the QHA to calculate their equilibrium lattice parameters at room temperature, whereas for other elements, such as Ca, Sr, Pb, Ce and Yb, which seem to exhibit non-negligible anharmonic behavior at room temperature, we used MD to calculate their lattice parameters for potential optimization. EAM potentials of the elements were optimized so that they produce equilibrium lattice parameters equal to experimental values at room temperature. Table III lists the lattice parameters of different elements derived from their optimized EAM potentials under different conditions.

The thermal behavior of the elements can be further explored by studying the coefficient of linear thermal expansion (CTE), which is given by:

$$\alpha(T) = \frac{1}{a_e(T)}\left(\frac{da_e(T)}{dT}\right)_P \qquad (6)$$

Often in experimental works, $a_e(T)$ is replaced by a_0 at a reference temperature (usually taken to be room temperature). To be consistent with experiments, we calculated the

linear thermal expansion coefficient using $\alpha(T) = \frac{1}{a_e(298K)}\left(\frac{da_e(T)}{dT}\right)_P$, based on both the QHA and MD calculations. The variation of the CTE with temperature is shown in Fig.4 for Au. For other fcc metals, the calculated and experimental CTE at room temperature can be found in Table III. The average discrepancy between the EAM calculation and experiment is found to be less than 10 percent, indicating that the as-developed EAM potentials are appropriate for the thermal expansion behavior of the metals near room temperature.

B. Mechanical properties

Adiabatic elastic constants C_{11}, C_{12}, and C_{44} of cubic metals can be evaluated from the second derivatives of the total Gibbs free energy with respect to strain,[63] and have the following form:

$$C_{ij} = \frac{1}{V}\left(\frac{\partial^2 E_{tot}}{\partial\varepsilon_i \partial\varepsilon_j}\right) + (P_{corr}) \qquad (7)$$

where the pressure correction term P_{corr} can be obtained using the equations derived by Barron and Klein:[64] For cubic systems under an applied pressure p, $P_{corr} = 0$ for C_{11}, $P_{corr} = p$ for C_{12} and $P_{corr} = -p/2$ for C_{44}.

The adiabatic elastic constants C_{11}, C_{12}, and C_{44} of Au were computed using the EAM potentials, as shown in Fig. 5. The three elastic constants increase rapidly as the lattice parameter (or volume) decreases. Under the adiabatic assumption, this phenomenon is consistent with the experimental observation that the elastic constants at 0 K (smaller lattice constant) are higher than those at room temperature for Au. The experimental elastic constants [65] corresponding to the two temperatures are also plotted in Fig.5 for comparison with EAM results.

Like the elastic constant tensor, other elastic moduli, such as the bulk modulus *K* and Young's modulus *Y*, contain information regarding the mechanical properties with respect to different modes of deformation. The bulk modulus *K* can be calculated from

the pressure-volume equation of state, as K is one of the curve parameters to describe the EOS. Under the condition of isotropic pressure, the fcc Au structure was compressed to different volumes at zero temperature employing the EAM model. The pressure-volume EOS plot is shown in Fig. 6. When the external pressure is less than ~100 GPa ($V/V_0 > 0.8$), the EOS curve derived from the EAM potential matched experimental data [66-68] very well, but when the applied pressure further increases, a noticeable deviation of the P-V curve from the shock-wave experimental data was identified. While more experimental data in the ultra-high pressure regime are desirable to validate the EAM model, the curvature of the EOS curve is, in principle, adjustable by decreasing the energy scale factor B in Eq. (2). In practice, however, this would have an unwanted effect on the melting temperature and the liquid density of Au, and therefore we decided not to pursue a perfect match between the calculated EOS and the high pressure experiments.

For cubic systems, the bulk and shear modulus, among other elastic moduli, can be conveniently derived from the three elastic constants C_{11}, C_{12}, and C_{44} based on the following relationships[69]:

$$K = (C_{11} + 2C_{12})/3 \tag{8}$$

$$G = (C_{11} + 3C_{44} - C_{12}) \tag{9}$$

$$Y = 9KG/(3K + G) \tag{10}$$

$$\nu = Y/(2G) - 1 \tag{11}$$

where G, ν are the shear modulus and Poisson's ratio, respectively. Using the above relationships, the variations of different elastic moduli as a function of lattice constant were computed, and the results are shown in Fig.5. One should be cautioned that the definitions for the moduli are not unique[70] and if different definitions/equations are assumed, the values of these moduli might be slightly different. Discretion should also be exercised if mechanical deformation is carried out under different conditions (e.g., an isothermal condition in lieu of the adiabatic condition).

Similar to Au, the elastic constants together with other elastic moduli have been derived for the fcc metals using the optimized EAM potentials. Those data are juxtaposed with experimental data in Table V for scrutiny. For softer materials such as Ca, Sr, Pb, Ce, and

Yb, the errors are found to be relatively large, but for transition metals and Al, the match between experiment and EAM is generally satisfactory. The average discrepancy between EAM calculations and experiments are found to be less than 5 percent for transition metals and Al, except for Pd, Ir. Pd exhibits a low-temperature anomaly discussed elsewhere,[75] and Ir shows a negative Cauchy pressure ($C_{44} > C_{12}$) in experiment, which presumably goes against the penalty paid for $F''(\rho) > 0$ during potential fitting.

C. Equations of state of six crystal structures

Employing the EAM, we evaluated the EOS (energy vs. volume) for 6 distinct crystal structures, which are fcc, hcp, 9R, bcc, sc, and dc structures, respectively. Fig. 7 shows the EOS of the 6 structures as a function of volume for Au. Also shown in Fig. 7 are *ab initio* calculations of those structures at selected volumes. For other metals, similar plots have also been derived. [28] Compared with *ab initio* data, the EAM potentials provide very good EOS results for close-packed structures, such as fcc, hcp and 9R, but slightly worse fitting results for open structures such as sc and dc. For each metal, we compared the formation energies of different structures relative to the fcc structure, calculated with the EAM potentials (the results can be found in Table VI). For all the metals studied in the current work, the EAM potentials correctly predict the fcc structure as the ground state. Both the *ab initio* and EAM calculations yield the relative stability of the different crystal structures in the following order: fcc, hcp or 9R, bcc, sc and dc. It should be mentioned that all the EAM potentials developed for the metals can correctly differentiate the fcc and hcp atomic environments at the ground states, despite the fact that the two structures have the same coordination number. The formation energy differences between fcc, hcp, and bcc lattices are comparable with experimental calculations, suggesting that the as-developed EAM potentials are sufficient in predicting crystal stability. For Au, the energy difference between fcc and bcc crystals, or, the relative stability of the two crystal structures, can be further reflected from the deformation path studies as shown in Fig. 9 and Fig. 10.

D. Crystal defects

a. Point defects

The formation energy of vacancies was calculated by minimizing the total energy of an fcc configuration containing a single vacancy using both the *ab initio* and EAM methods. The finite size effect was minimized by increasing the size of the simulation system. EAM calculation yields the formation energy of 0.98 eV for a single Au vacancy, which agrees very well with other cited values of 0.89-1.00 eV. [90] The migration energy of the vacancy, which is the energy barrier for vacancies to diffuse and is deemed important for deformation and melting, was calculated using the nudged elastic band method.[83] The vacancy migration energy is found to be 0.79 eV, consistent with the experimental vacancy migration value for Au (0.78~0.88 eV). Using the same method, vacancy formation energies and migration energies were evaluated for other fcc metals employing the optimized EAM potentials, as listed in Table VII. The values estimated by the EAM potentials yield reasonable agreement with the experiment. In addition to vacancies, we also considered numerous interstitial point defects during potential fitting: tetrahedral interstitials, octahedral interstitials, and dumbbell interstitial defects along the [100], [110], [111] directions. Experimental data on those defects are not available; nonetheless, formation energies of these defects are still listed in Table VII for future reference, which are comparable with *ab initio* calculations in the current work, within errors of about 0.05 eV.

b. Surface energies

One common problem with the EAM is that this method often underestimates the surface energies. In the current work, we have seen improvement of the newly developed potentials over previous EAM models in describing surface energies. Formation energy of three low-index crystal surfaces was evaluated for all the metals, and in each case the surface structures were fully relaxed with MD, but without surface reconstruction. Our EAM calculations yield the correct order of the formation energy of the three surfaces: (111) < (100) < (110). The three surface energies γ_{111}, γ_{100}, γ_{110} for Au is found to be 1151 mJ/m^2 , 1222 mJ/m^2 and 1301 mJ/m^2, respectively. The average surface energy of Au is around 1500 mJ/m^2 from the experiment. Surface energy values, as predicted by the

current EAM models, are listed in Table VIII. While accurate measurements of the surface energy values are needed, the potentials may still slightly underestimate the surface energies as they stand, as seen from Table VIII.

As is well known, late transition metals, notably Ir, Pt, and Au, exhibit surface reconstructions;[104-106] for these metals, the surface reconstruction phenomena are typified by the missing-row (1x2) surface reconstruction of (100), and the quasi-hexagonal surface reconstruction of (100). In the current work, our preliminary results on Au demonstrate that the EAM model is able to predict both the Au (110) missing-row and Au (100) quasi-hexagonal surface reconstructions. Further in-depth research work along this direction is current under way.

c. Planar defects

It is understood that stacking fault energy and unstable stacking fault energy are important quantities determining the mechanical behavior of metals, and the γ surface [107] technique can help to assess these types of stacking faults. The γ surface, or the generalized-stacking-fault energy surface, can be formed by rigidly shifting (111) atomic planes along directions composed of perpendicular $[0\bar{1}0]$ and $[12\bar{1}]$ directions, as schematically illustrated in Fig.8a. Employing the EAM model, the γ surface of fcc-Au (4.078 Å) was calculated, as shown in Fig. 8b. To validate the EAM results, we compared them with *ab initio* calculations of the GSF along $[0\bar{1}0]$ and $[12\bar{1}]$ directions. For *ab initio* calculations, 12 layers of (111) planes were stacked together forming a fcc lattice with periodic conditions. The upper part of the fcc lattice was gradually shifted along the $[12\bar{1}]$ direction, creating two stacking faults with opposite directions: $\{111\}<\bar{1}\bar{2}1>$ and $\{111\}<12\bar{1}>$. The total formation energy of the stacking faults was plotted along the displacement of the (111) plane. Similarly, GSF along the $[0\bar{1}0]$ direction was also created. The GSF energy was calculated and plotted against the displacement of the (111) atomic planes. At the maxima of the curves, it was found that the average difference between *ab initio* and EAM calculations is less than 5 percent.

In addition to the GSF, we also studied the Au intrinsic stacking fault and Au(111) twinning defects, as both are found important in governing the mechanical properties and

deformation mechanisms of metals. For both defect types, the coordination number of the atoms on the defective planes is the same as those in perfect fcc lattices, which poses a challenge for EAM potentials to correctly produce the formation energies of the defects. Using the newly developed EAM potentials, we found that the predicted formation energies of the relaxed stacking faults are generally in agreement with experiments. For Au, the intrinsic stacking fault energy and the twinning fault energy are calculated to be 30 mJ/m^2 and 15 mJ/m^2, respectively, in comparison with the experimental values of 32 mJ/m^2 [26] for the intrinsic stacking fault energy. For other metals, the intrinsic stacking fault and twinning fault energies are tabulated in Table VIII. Generally speaking, the predicted intrinsic stacking fault energy and twinning energy are comparable with experimental values available in literature.

E. Deformation paths

Displacive transformations, referred to as lattice transformations connecting different metastable structures, are of particular interest in terms of understanding the mechanism of phase transformation, configurations of extended defects, the structure of epitaxial films, and so forth.[108] In this work, we considered two transformation paths in cubic structures of metals: a) the fcc-bcc tetragonal deformation path (i.e., the usual Bain deformation path); and b) the trigonal deformation paths.

a. Deformation along the bcc-fcc Bain path

The tetragonally deformed structures may be parameterized in terms of c/a ratio. Along the deformation paths, the initial fcc lattice $c/a = 1$ is compressed along a [001] direction and simultaneously expanded to an equal extent in [010] and [001] directions so as to preserve the atomic volume. The cohesive energy along the bcc-fcc path (shown in Fig. 9) was plotted against the c/a ratio for Au. The lattice becomes bcc when $c/a = \sqrt{2}/2$. Two configurations corresponding to the fcc and bcc structures along the deformation path are shown in the inset of Fig. 9. Both calculations employing the EAM and DFT methods predicate a local maximum of the energy at $c/a = \sqrt{2}/2$, thus indicating that the bcc structure is unstable against tetragonal deformation. This instability is consistent

with the negative shear modulus found for the bcc structure. The shallow minimum observed at $c/a =\sim 0.6$ corresponds to a body-centered tetragonal (bct) structure which is meta-stable against tetragonal distortions but is unstable against other modes of deformation [88] (see below). All other metals studied in the current work exhibit the same behavior. In fact, for all metals studied, the energy surfaces of fcc metals for the tetragonal deformation mode exhibit two energy minima, corresponding to the aforementioned fcc and sc structures connected by a saddle point, where the energy is the maximum (bcc). Energy contours of the energy surface corresponding to different volume and c/a ration are shown in Fig.9 b for Au.

b. Deformation along the trigonal Bain path

In the trigonal Bain deformation path, one changes the interplanar distance between the (111) planes, while maintaining the tri-fold symmetry around the [111] axis. To study this deformation, the atomic volume of the lattice was preserved, and consequently, the angle between the three primitive basis vectors, θ, changed with the degree of trigonal deformation. In the case of Au, the energy of the lattice was evaluated using the EAM and DFT methods, and plotted against θ. Along the trigonal deformation path, one can easily identify three lattice structures: fcc ($\theta = 60^o$), sc ($\theta = 90^o$), and bcc ($\theta = 109.45^o$). The evolution of the lattice along the trigonal deformation path was depicted in the inset of Fig.10. Indeed, the energy profile evaluated using the EAM model exhibits three extrema at the three angles. This is consistent with the *ab initio* calculations. Corresponding to the minima on the energy profile are two metastable crystal structures: fcc and bcc, connected by a saddle point corresponding to the sc structure. The maximum energy of the sc structure indicates that this structure is unstable against trigonal deformation. Therefore, the relative meta-stability of the three phases can be captured by the EAM models developed here.

F. Liquid structures

In the current work, special attention has been given to the capability of EAM potentials to describe liquid metals by enforcing a fit to a large amount of liquid data on the PES. We started by analyzing the melting temperature of the crystals. The melting temperature

of the metals was calculated using the two-phase coexisting method with MD computer simulation.[110] We obtained the melting temperature for Au to be 1320±15 K employing the current EAM potential model, which is close to the experimental melting point of Au, 1337K. It should be noted that the melting temperature was not explicitly included in potential fitting in the present work. The EAM-predicted melting temperature is highly correlated to the EOS of the crystal. Incidentally, in a recent work a non-linear scaling method was applied to the Rose type of EOS for gold, and was found successful in improving the T_m of Au [27]. Compared to the experimental melting enthalpy of Au (12.6 kJ/mol) and volume change upon melting ($\Delta V_m / V_c = 5.1\%$), theoretic work yields the melting enthalpy (11.1 kJ/mol) and melting volume change (4.9%) for Au. It is thus evident that the capability of the current EAM model to predict melting behavior is on par with the second NN-MEAM potentials for Au. [26,27] Likewise, the melting temperatures for other metals, together with their evaluated melting enthalpies and volume changes upon melting, have also been calculated and tabulated in Table IX for comparison with experimental data.

In the current work, the PES was rescaled to match the experimental liquid density within an error of ~1.0%, which is about the uncertainty of most liquid density measurements in a given experiment. Fig. 11 shows the density change of Au during the melting and cooling process in an MD computer simulation. Compared with other potential models[6,26,105] for liquid Au, the liquid densities resulting from the current model are in excellent agreement with the experimental data. The estimated densities for other metals at their melting temperatures are listed in Table IX. In all cases, the theoretic liquid densities are within 1.0 percent of their experimental values at their melting points.

The liquid structures were further investigated by examining their static structure factors $S(Q)$ and radial distribution functions (RDF) $g(r)$ at various temperatures. Both quantities can be computed using textbook methods.[124-126] Fig. 12a illustrates the evolution of $g(r)$ as a function of the temperature at which liquid Au was equilibrated. With decreasing temperature, the intensity of the first peak of the RDF increases and the peak width slightly broadens. The static structure factor $S(Q)$, on the other hand, is a Fourier transform of the RDF, and can be experimentally extracted. Theoretic $S(Q)$ of

liquid Au was computed and plotted in Fig.12b at different temperatures to show their evolution. Experimentally, Waseda et al.,[127] has systematically measured the structure factors for different liquid metals by means of X-ray diffraction, which provides a benchmark for validating our EAM models. However, by comparing with newer structural data, it has been recognized [126] that, in Waseda's $S(Q)$ data, the peak intensities were systematically underestimated. Therefore, in order to compare our simulated $S(Q)$ with experiments, a decay factor of $e^{-\zeta q^2}$ (usually $0 < \zeta < 0.2$ and q is the wave vector) was applied to $S(Q)$ to account for experimental uncertainties. Fig. 13c shows the calculated and experimental $S(Q)$ for Au at 1423 K. A satisfactory agreement between the experiment and the potential model can be found in terms of peak position, intensity, and shape. In fact, for other liquid metals, except Pb and Yb, the overall matches between the EAM $S(Q)$ and experimental data are satisfactory.

G. Liquid dynamics

In order to study liquid dynamics using the EAM models, we focused on the transport properties of the liquids. Two complementary methods[124-126] were used to derive their self-diffusion coefficients. The first method is based on Einstein's formula:

$$D = \lim_{t\to\infty} \frac{\left\langle \Delta r^2(t) \right\rangle}{6t} \tag{12}$$

where $\left\langle \Delta r^2(t) \right\rangle$ is the mean-square displacement of tagged particles.

The second method is based on the Green-Kubo relation, in which the coefficient is given as the time integral of a time-dependent correlation function:

$$D = \frac{k_B T}{m} \int_0^\infty C(t)dt\,, \tag{13}$$

where $C(t) = \left\langle \mathrm{v}(t)\mathrm{v}(0) \right\rangle / \left\langle v^2 \right\rangle$ is the normalized velocity auto-correlation function and k_B is the Boltzmann constant, T denotes temperature, and m is the mass of particles. At different temperatures, the MSD and velocity self-autocorrelation functions of Au at different temperatures were computed with MD simulations (4000 atoms in NVE

ensembles of well-equilibrated liquids), as shown in Fig. 13 a and b. Consequently, the self-diffusion coefficient of Au was computed using Eq. (12) and (13) respectively, and plotted in Fig.12b as a function of temperature. Similarly, the self-diffusion coefficients of other metals at desired temperatures were estimated using both the Einstein relation (D^E) and the Green-Kubo relation (D^{GK}), as listed in Table IX. Also listed are the self-diffusion coefficients available from experiments. It can be seen that the values of the diffusion constant *D* computed using the Green-Kubo and Einstein relations are generally consistent with each other. For the metals whose self-diffusion coefficients (Cu, Ag, Pb) are available in literature, our computed values of this transport coefficient are in firm agreement with the experimental results.

The dynamic properties of the metallic liquids can be further studied by assessing van Hove's time-dependent pair correlation function: [128]

$$G(r,t) = \frac{1}{N}\sum_{i=0}^{N}\left\langle \delta(r - (\mathrm{r}_i(t) - \mathrm{r}_i(0)\right\rangle . \qquad (14)$$

It should be noted that here we are only concerned with the self-part of the van Hove correlation function for the monatomic liquids. Usually it is easier to work with the transformed van Hove function $4\pi r^2 G(r,t)$. In Fig. 14a we show $4\pi r^2 G(r,t)$ of Au near the melting temperature (1500K). Related to the van Hove pair correlation function are its two Fourier transforms: its spatial Fourier transform with respect to *r* termed "intermediate scattering function" $F(q,t)$, and its temporal and spatial Fourier transform called "dynamic structure factor" $S(q,\omega)$. Both functions contain rich information about particle correlation and time evolution, which can be directly measured via experimentation. For elements with available dynamic structure factor data, such as Ni, Al and Pb,[129] the simulated $S(q,\omega)$ or $F(q,t)$ match well with experimental data. Unfortunately, experimental data on the dynamical structure factors are not available for Au. Nonetheless, we plot the dynamical structural data of Au at 1500 K in Fig. 14b for the completeness of the present work.

IV Conclusion

Highly optimized EAM potentials have been developed for 14 fcc metals using the PES-fitting method. For each element, we first established a first-principles database to include several hundreds of atomic configurations. High-precision *ab initio* calculations of those configurations form the PES of the systems. The PES was deformed by linear scaling to match experimental data: lattice parameter at room temperature, cohesive energy, and liquid density at the melting point. The revamped PES, together with accurate experimental data on elastic constants and phonon frequencies, was used to optimize the EAM potentials. Through studying the lattice dynamics, thermal expansion, defects, deformation paths, melting behavior and liquid properties, the as-developed potentials were shown to have high fidelity and wide applicability.

In the present work, the cutoff distance of the EAM models is relatively large compared to recently proposed modified-EAM potentials with angular terms[130]. This "long distance description" might be a surrogate for the "angular description". It is true that real interaction chemistry works at short distances and is sensitive to angles. This is probably why some surface properties are less well reproduced by the current potentials than most properties in the bulk. We believe the current fitting strategy is applicable to constructing potentials with more explicit chemistry such as modified EAM[130], angular dependent potential models (ADP)[131], and bond-order potentials (BOP)[132]. The established EAM potentials of the elements, however, are believed to find wide applications in diverse areas of materials science and engineering. Due to the "*ab initio*" nature of the as-developed potentials, they are suitable to link atomistic computer simulations with high-level quantum mechanics calculation to form advanced multi-scale simulation platforms.[133]

Acknowledgement

The authors thank Y. Mishin and M.I. Baskes for helpful discussions. This work is supported by U.S. NSF under Grant No. DMR-0907325, U.S. Department of Energy by Iowa State University under Contract No. DE-AC02-07CH11358, and ONR under Grant N00014-09-1-1025A. HWS, FT and MWC acknowledge use of the supercomputing

system at the Center for Computational Materials Science, Institute for Materials Research, Tohoku University.

References:

1. D. Wales, Cambridge University Press (2003)

2. J. Hafner, C. Wolverton, G. Ceder, MRS Bulletin 31, 659 (2006)

3. A.R. Leach, *Molecular Modeling: Principles and Applications*, Prentice Hall (2001)

4. D. Frenkel and B. Smit, *Understanding Molecular Simulation*, Academic Press (1996)

5. M.S. Daw, M.I. Baskes, Phys. Rev. B 29, 6443 (1984)

6. S.M. Foiles, M.I. Baskes, M.S. Daw, Phys. Rev. B 33, 7983 (1986)

7. R.A. Johnson, Phys. Rev. B 39, 12554 (1989)

8. Y. Mishin, D. Farkas, M.J. Mehl., et al., Phys. Rev. B 59, 3393 (1999)

9. W. Kohn, Phys. Rev. 140, 1133 (1965)

10. M.W. Finis and J.E. Sinclair, Phil. Mag. A 50, 45 (1984)

11. A.P. Sutton and J. Chen, Phil. Mag. 61, 139 (1990)

12. G.J. Ackland and V. Vitek, Phys. Rev. B 41, 10324–10333 (1990)

13. F. Cleri and V. Rosato, Phys. Rev. B 48, 22 (1993)

14. K.W. Jacobsen, J.K. Norskov, M.J. Puska, Phys. Rev B 35, 7423 (1987)

15. F. Ercolessi, J.B. Adams, Europhys. Lett. 26, 583 (1994)

16. J. D. Gale and A. L. Rhoh, *The general utility lattice program (GULP),* Molecular Simulation 29, 291 (2003)

17. P. Brommer, F. Gahler, Modeling and Simulation in Materials Science and Eng. 15, 295 (2007)

18. J. Behler and M. Parrinello, Phys. Rev. Lett. 14, 146401 (2007)

19. T.J. Lenosky, B. Sadigh, E. Alonoso, V.V. Bulatov, *et al*, Modelling Simul. Mater. Sci. Eng. **8,** 825 (2000)

20. Y.Q. Cheng, E. Ma, and H.W. Sheng, Phys. Rev. Lett., 102, 245501 (2009)

21. A.T. van Duin, S. Dasgupta, F. Lorant, W.A. Goddard III, J. Phys. Chem *A*, *105*, 9396 (2001)

22. M.R. Felliinger, H. Park, J.W. Wilkins, Phys. Rev. B 81, 144119 (2010)

23. Y. Kimura, Y. Qi, T. Cagin, and W.A. Goddard III, MRS Symposium Ser. 554 (1999)

24. S. Oliver, R. Conte and A. Fortunelli, Phys. Rev. B 77 054104 (1994)

25. B.J. Lee, J.H. Shim and M.I. Baskes, Phys. Rev. B 68, 144112 (2003)

26. G. Grochola, S. P. Russo, and I. K. Snook, J. Chem. Phys. 123, 204719 (2005)

27. S. Ryu, C. R. Weinberger, M. I. Baskes and W. Cai, Modelling Simul. Mater. Sci. Eng. **17** 075008 (2009)

28. http://sites.google.com/a/gmu.edu/eam-potential-database/Home

29. S. J. Plimpton, J. Comp. Phys, 117, 1-19 (1995)

30. J. Roth, F. Gähler, and H.-R. Trebin, Int. J. Mod. Phys. C 11, 317-22 (2000).

31. W. Smith; C. W. Yong; P. M. Rodger, Molecular Simulation, 28, 385 (2002)

32. J. Rifkin, *XMD Molecular Dynamics Program*, University of Connecticut (2002)

33. G. Kress, and J. Hafner, Phys. Rev. B 49, 14251 (1994)

34. P.E. Blöchl, Phys. Rev. B 50, 17953 (1994).

35. G. Kresse, and J. Joubert, Phys. Rev. B 59, 1758 (1999).

36. H. J. Monkhorst and J. D. Pack, Phys. Rev. B **13**, 5188 _1976

37. J.G. Herriot and C.H. Reinsch, ACM TOMS 9, 258-259, (1983) http://www.netlib.org/toms/600

38. W.H. Press, S.A. Teukolsky, W.T. Vetterling and B.P. Flannery, *Numerical Recipes 3rd Edition, The art of Scientific Computing*, Cambridge University Press (2007)

39. S. M. Foiles and M. S. Daw, Phys. Rev. B 38, 12643 (1988)

40. Q.B. Bian, S.K. Bose and R.C. Shukla, J. Phys. Chem. Solids, 69, 168 (2008)

41. M.T. Dove, *Introduction to lattice dynamics*, Cambridge University Press (2007)

42. J.W. Lynn, H.G. Smith, and R.M. Nicklow, Phys. Rev. B 8, 3493–3499 (1973)

43. http://www.quantum-espresso.org The PWSCF phonon calculation was carried out with the GGA and an ultrasoft pseudopotential for Au. Monkhorst-pack 11x11x11 kpoint grids were used for the Brillion zone integration. The lattice parameter for the phonon calculation (a0=4.123 Å) was obtained by geometric optimization.

44. http://cst-www.nrl.navy.mil/bind/kpts/fcc/.

45. J. Bandopadhyay and K.P. Gupta, Cryogenics 18, 54 (1978)

46. F.R. Kroeger, J. Appl. Phys. 48, 853 (1977)

47. H.W. King and F.D. Manchester, J. Phys. F: Met. Phys. 8 15 (1978)

48. M.E. Straumanis and C.L. Woodward, Acta Crystallogr. A27 549 (1971)

49. Y.S. Touloukian, R.K. Kirby, R.E. Taylor, P.D. Desai, *Thermal Expansion, Metallic Elements and Alloys*, Plenum Press, New York (1975)

50. R. Stedman and G. Nilsson, Phys. Rev. 145, 492 (1966)

51. R. J. Birgenau, J. Cordes, G. Dolling, and A. D. B. Woods, Phys. Rev. 136 A1359 (1964)

52. G. Nilsson and S. Rolandson, Phys. Rev. B 7, 2393 (1973)

53. A. Eichler, K.P. Bohnen, W. Reichardt, and J. Hafner, Phys. Rev. B57, 324 (1998)

54. A.P. Miller and B.N. Brockhouse, Phys. Rev. Lett, 20, 798 (1968)

55. W.A. Kamitakahara and B.N. Brockhouse, *Phys. Lett.* **29A, 639** (1980)

56. R. Heid, K-P Bohnen, K. Felix, K. M. Ho and W. Reichardt, J. Phys. Cond. Matter 10, 7967 (1998)

57. D.H. Dutton, B.N. Brockhouse, and A.P. Miller, Can. J. Phys. 50, 2915 (1972)

58. C. Stassis, J. Zaretsky, D.K. Misemer, H.L. Skriver, B.N. Harmon and R.M. Nicklow, Phys. Rev. B 27, 3303 (1983)

59. U. Buchenau, M. Heiroth, H.R. Schober, J. Evers and G. Oehlinger, Phys. Rev. B30, 3502 (1984)

60. R. Stedman, L. Almqvist, G. Nilsson, and G. Raunio, Phys Rev. 162, 545 (1967)

61. C. Stassis, T. Gould, O.D. Mcmasters, K.A. Gschneidner Jr. and R.M. Nicklow, Phys. Rev. B 19 5476 (1979)

62. C. Stassis, C.K. Loong, C. Theisen, and R.M. Nicklow, Phys. Rev. B 26, 4106 (1982)

63. C.R.A. Catlow, *Computer Modeling in Inorganic Crystallography*, Academic Press (1997)

64. T.H.K. Barron and M.L. Klein, Proc. Phys. Soc. 85, 533 (1965)

65. G. Simons and H. Wang, Single Crystal Elastic Constants and Calculated Aggregate Properties (MIT Press, Cambridge, MA, 1977)

66. M. Yokoo, M. Kawai, K.G. Nakamura, K. Kondo, Y. Tange, and T. Tsuchiya, Phys. Rev. B 80, 104114 (2009)

67. M. Matsui, J. Phys. Conf. Series 215, 012197 (2010)

68. R.G. McQueen and S.P. Marsh, J. Appl. Phys. 31, 1253 (1960)

69. Y.C. Fung, *First course in continuum mechanics*, 3rd ed. Prentice Hall (1993)

70. J.F. Nye, Physical properties of crystals, Oxford Press (1957)

71. A.M. James and M.P. Lord in *Macmillan's Chemical and Physical Data*, Macmillan, London, UK, (1992)

72. G.W.C. Kaye and T. H. Laby in *Tables of physical and chemical constants*, Longman, London, UK, 15th edition, (1993)

73. G.V. Samsonov (Ed.) in *Handbook of the physicochemical properties of the elements*, IFI-Plenum, New York, USA, (1968)

74. http://www.answers.com/topic/rhodium

75. R. J. Wolf, K. A. Mansour, M.W. Lee and J. R. Ray, Phys. Rev. B 46, 8027–8035 (1992)

76. A.S. Darling. Journal of the Institute of Metals. (1966)

77. M.S. Anderson, C.A. Swenson, and D.T. Peterson, Phys. Rev. B 41, 3329 (1990)

78. E.A. Brandes and G.B. Brook, *Smithells Metals References Book* (7th edition, Oxford, Butterworth-Heinemann)

79. N. Singh and S.P. Singh, Phys. Rev. B 42, 1652 (1990)

80. A.T. Dinsdale, CALPHAD: Comput. Coupling Phase Diagrams Thermochem. **15**, 317 (1991)

81. J.E. Hearn, R.L. Johnson, S.L. Leoni and J.N. Murrel, J. Chem. Soc., Faraday Trans., 92, 425 (1996)

82. H.L. Skriver, Phys. Rev. Lett., 49, 1768 (1982)

83. G. Henkelman and H. Jónsson, J. Chem. Phys., 113, 9978-9985, (2000)

84. B. L. Eyre, *Crystals: Point Defects in Encyclopedia of Materials: Science and Technology*, UNIVERSITY OF OXFORD, UK (2001)

85. H.-E. Schaefer, R. Gugelmeier, M. Schmolz, and A. Seeger, Mater. Sci. Forum **15-18**, 111 (1987)

86. R. W. Balluffi, J. Nucl. Mater. **69&70** 240 (1978)

87. W. Wycisk and M. Feller-Kniepmeier, J. Nucl. Mater. **69/70**, 616 (1978)

88. Y. Mishin, M. J. Mehl, D. A. Papaconstantopoulos, A. F. Voter and J. D. Kress, Phys. Rev. B 63, 224106 (2001)

89. F. R. de Boer, R. Boom, W. C. M. Mattens, A. R. Miedema, and A. K. Niessen, *Cohesion in Metals* (North-Holland, Amsterdam, 1988, vol. 1)

90. J.J. Wollenberger, *Physical Metallurgy,* edited by R.W. Cahn and P. Hansen (Amsterdam, North-Holland, 1983), p.1139

91. P.L. Williams, Y. Mishin and J.C. Hamilton, Modelling Simul. Mater. Sci. Eng. 14, 817 (2006)

92. P. Ehrhart, in *Vacancies and Interstitials in Metals*, edited by A. Seeger, D.

Schumacher, W. Schilling, and J. Diehl, North-Holland, Amsterdam, p. 363 (1970)

93. L. E. Murr, *Interfacial Phenomena in Metals and Alloys* Addison-Wesley, Reading, MA, (1975)

94. W. R. Tyson and W. R. Miller, Surf. Sci. **62**, 267 (1977)

95. H.L. Skriver and N.M. Rosengaard, Phys. Rev B 46, 7157 (1992)

96. L.Z. Mezey and J. Giber, *Jpn. J. Appl. Phys., Part 1* **21**, 1569 (1982)

97. R. H. Rautioaho, Phys. Status Solidi B **112**, 83 (1982)

98. K. H. Westmacott and R. L. Peck, Philos. Mag. **23**, 611 (1971)

99. C. B. Carter and I. L. F. Ray, Philos. Mag. **35**, 189 (1977)

100. N. M. Rosengaard and H. L. Skriver, Phys. Rev. B 47, 12 865 (1993)

101. C.S. Barrett and T.B. Massalski, *Structure of Metals,* McGraw- Hill, New York (1966)

102. Y.N. Gornostyrev, M.I. Katsnelson, N.I. Medvedeva, O.N. Mryasov, A.J. Freeman, and A.V. Trefilov, Phys. Rev. B 62, 7803 (2000)

103. M.J. Cawkwell., D. Nguyen-Manh, D. G. Pettifor and V. Vitek.., Phys. Rev. B 73, 064104 (2006)

104. M.I. Haftel, Phys. Rev. B 48, 2611–2622 (1993)

105. F. Ercolessi, M. Parrinello, and E. Tosatti, Philos. Mag. A **58**, 213 (1988)

106. K. Oura, V.G. Lifshits, A.A. Saranin, A.V. Zotov and M. Katayama, *Surface Science: An Introduction*. Berlin: Springer-Verlag (2003)

107. V. Vitek, *Phil. Mag.* 18, p. 773(1968)

108. M. Sob, L.G. Wang and V. Vitek, Comp. Mater. Sci. 8, 100 (1997)

109. S.Yoo, X.C. Zeng, J.R. Morris, J. Chem. Phys, 120, 1655 (2004)

110. F. C. Campbell, *Elements of metallurgy and engineering alloys*, ASM International (2008)

111. E. G., T. Iida and R. I. L. Guthier, *The Physical Properties of Liquid Metals* (Clarendon, Oxford, 1988).

112. M.J. Assael, et al., Journal of Physical and Chemical Reference Data, 35, (1), 285-300 (2006)

113. A.V. Gorshkov, Inorganic Materials, 2, 218 (2000)

114. P. Protopapas, H.C. Andersen, and N.A.D. Parlee, J. Chem. Phys. 59, 15 (1973)

115. M.M.G. Alemany, O. Diéguez, C. Rey and L.J. Gallego, Phys. Rev. B 60, 9208 (1999)

116. P-F. Paradis, T. Ishikawa, Y. Saita, and S. Yoda, International Journal of Thermophysics, 25, 1905 (2004)

117. P.F. Paradisa, T. Ishikawa, and N. Koike, Gold Bulletin, 41, 242-245 (2008)

118. L.W. Wang, Q. Wang, A.P. Xian and K.Q. Lu, J. Phys.: Condens. Matter 15 777 (2003)

119. T.Ishikawa, P. Paradis and N. Koike, Jap. J. Appl. Phys. 45, 1719 (2006)

120. S. Hiemstra, D. Prins, G. Gabrielse and J. B. Van Zytveld, Physics and Chemistry of Liquids, 6, 271 (1977)

121. T. Ishikawa, P.-F. Paradis,1 R. Fujii, Y. Saita, and S. Yoda, International Journal of Thermophysics, 26, 893 (2005)

122. J. Brillo and I. Egry, Int. J. Thermo. 24, 1155 (2003)

123. P.F. Paradis, T. Ishikawa, and S. Yoda, International journal of thermophysics 24,1121-1136 (2003)

124. M.P. Allen and D.J. Tildesley, *Computer Simulation of liquids*, Oxford University Press, Oxford, 1990

125. J.P. Hansen and I.R. McDonald, *Theory of Simple Liquids*. Academic Press. (1986)

126. M.M.G. Alemany, C. Rey and L.J. Gallego, Phys. Rev. B 58, 685 (1985).

127. Y. Waseda, *The Structure of Non-Crystalline Materials* (McGraw-Hill, New York, 1980).

128. L. van Hove, Physical Review **95**, 249(1954)

129. T. Scopigno, G. Ruocco, and F. Sette, Rev. Mod. Phys. **77**, 881 (2005)

130. M.I. Baskes, *Phys. Rev.*B **46**, 2727(1992)

131. Y. Mishin et al., Acta Mat **53**, 4029 (2005)

132. D.G. Pettifor and I. I. Oleinik, Phys. Rev. **B 59 (1999)**.

133. N.M. Ghoniem, E.P. Busso, N. Kioussis, et al., Phil. Mag., 83, 3475 (2003)

Figure Captions:

Figure 1 EAM potential plots for Au. The three plots show the slowly varying profiles of the pair function $\phi(r)$, density function $\rho(r)$ and the embedding function $F(n_i)$, respectively, in Eq (1).

Figure 2 Comparison of phonon-dispersion curves of Au predicted by the present EAM potential with the experimental values measured by neutron diffraction at 80 K. The phonon frequencies at point *X* were included in the potential fit. Also shown is the *ab initio* calculation using PWSCF. [43] ([a]Ref. 42 and [b]Ref. 43).

Figure 3 Lattice constant of Au as a function of temperature predicted using the present EAM model. Both the QHA and MD methods were used for the evaluation of the equilibrium elastic constants at different temperatures. The importance of the quantum effect is also shown in the plot by excluding the zero point energy in Eq. (4) in obtaining the lattice constant (see text).

Figure 4 Linear thermal expansion coefficient of Au as a function of temperature.

Figure 5 Adiabatic elastic constants of Au as a function of lattice constants (solid lines), as predicted by the EAM. Also obtained are other important elastic moduli shown in the plot. Experimental elastic constants at two temperatures are shown for comparison.

Figure 6 Pressure-volume EOS of Au at T=0 calculated using the EAM model in comparison with experimental data. [67-68]

Figure 7 Comparison of *ab initio* and EAM calculations of the cohesive energies of six different crystal structures of Au at different volumes.

Figure 8 EAM calculations of the γ surface of Au on the (111) plane. (a) Schematic drawing showing the displacements of the (111) plane to obtain the γ surface; (b) EAM calculation of the γ surface; (c) Comparison of the EAM and ab initio calculations of GSF energy displaced along the $[0\bar{1}0]$ direction (unit: $\frac{\sqrt{2}}{2}a$); Comparison of the EAM and ab initio calculations of GSF energy displaced along the $[12\bar{1}]$ direction (unit: $\frac{\sqrt{6}}{2}a$) (see text).

Figure 9 (a) Comparison of EAM and *ab initio* calculations of energy along the tetragonal Bain path between fcc and bcc structures. Calculations were performed at a constant volume corresponding to the equilibrium fcc phase. (b) Contour plot of the PES for centered tetragonal Au as a function of c/a and the reduced volume Ω/Ω_0. The contour spacing is 5 meV.

Figure 10 Comparison of EAM and *ab initio* calculations of energy along the trigonal Bain path between fcc, sc and bcc structures. Calculations were performed at a constant volume corresponding to the equilibrium fcc phase.

Figure 11 Density changes of Au during melting and freezing, as obtained from NPT molecular dynamics simulations (32,000 atoms) employing the present EAM potential. ([a]Ref. 117, [b]Ref.111)

Figure 12 (a) The evolution of RDF of liquid Au at different temperatures employing the EAM potential; (b) Structure factor $S(Q)$ of Au as a function of temperature; (c) Comparison of experimental[127] and theoretical $S(Q)$ of liquid Au near the melting point.

Figure 13 (a) MSD of liquid Au during molecular dynamics equilibration at different temperatures. (b) Velocity auto-correlation functions of liquid Au at different temperatures. (c) Self-diffusion coefficient of Au at different temperatures, as derived from the Einstein and the Green-Kubo methods.

Figure 14 Dynamical properties of Au examined by means of (a) the van Hove self auto-correlation function; (b) self-intermediate scattering function of Au. Both plots were plotted against time to show their dynamical evolution (see text).

Table I Valence electron configurations of the elements applied in the *ab initio* calculations in the present work. A and B are two unitless scaling factors to deform the PES according to Eq. (2).

	Electron configuration	A	B	C (eV)
Al	$3s^2 3p^1$	0.9916	1.000	0.3255
Ni	$3d^8 4s^2$	0.9959	1.000	0.9614
Cu	$3d^{10} 4s^1$	0.9891	1.000	0.1913
Rh	$4d^8 5s^1$	0.9862	1.023	1.6340
Pd	$4d^{10} 5s^0$	0.9797	1.050	1.8198
Ag	$4d^{10} 5s^1$	0.9782	1.239	0.5295
Ir	$5d^8 6s^1$	0.9900	1.062	2.3950
Pt	$5d^9 6s^1$	0.9808	1.130	1.2325
Au	$5d^{10} 6s^1$	0.9724	1.410	0.7137
Ca	$3p^6 4s^2$	1.0082	1.000	0.0722
Sr	$4s^2 4p^6 5s$	1.0034	1.100	0.1277
Pb	$6s^2 6p^2$	0.9818	1.100	1.1150
Ce	$s^2 d^1 f^1$	0.9665	1.000	0.4127
Yb	$5p^6 6s^2$	1.0122	1.000	0.2359

Table II. Predicted values of interatomic potential models compared with experimental properties. The numbers in parentheses are the fitted experimental data.

Property	Exp.	Present	Glue Model [a]	Johnson[b]	FBD[c]	GRS[d]	MEAM[e]
Cohesive energy E_c (eV)	-3.93[f]	-3.93 (-3.93)	-3.78 (-3.78)	-3.930 (-3.93)	-3.927 (-3.93)	-3.924 (-3.93)	-3.93 (-3.93)
Lattice constant (Å)	4.078[f]	4.078 (4.078)	4.704 (4.07)	4.0806 (4.08)	4.0805 (4.08)	4.0701 (4.07)	4.073 (4.073)
Bulk Modulus (GPa)	180.3[g]	178.0	180.4	169.9 (167)	166.7 (167)	180.3	180.3
C_{11}-C_{12} (GPa)	32[g]	32 (30)	60 (32)	27 (29)	25 (29)	32 (32)	32 (32)
C_{44} (GPa)	45[g]	45 (42)	60 (45)	41 (42)	45 (42)	46 (45)	45 (45)
γ_{110} (relaxed) (mJ/m^2)	---	1321	1984	867	989	1533	1179
γ_{100} (relaxed) (mJ/m^2)	---	1261	2059	814	926	1296	1138
γ_{111} (relaxed) (mJ/m^2)	---	1194	1548	705	796	1196	928
Average γ_g (mJ/m^2)	1506[h]	1260	1863	795	904	1342	1081
E_v^f (eV)	0.89 ~1.00[i]	0.98	1.237	0.86	1.04	1.13	0.90
E_{SF} (mJ/m^2)	32[j]	30	0	---	---	42.6	40
Melting point (K)	1337[k]	1320	1338	1053	1121	1159	1410
$E_{bcc} - E_{fcc}$ (eV)	0.04[l]	0.04	0.045	0.0225	0.0206	0.0608	0.06
$E_{hcp} - E_{fcc}$ (eV)	0.003[l]	0.007	0	-0.00085	0.0011	0.0095	0.009
Liquid density 1500K (g/cm^3)	17.1[m]	17.1	18.3	16.7	17.2	17.3	---

[a]Ref. 105 ; [b]Ref.7; [c]Ref.6; [d]Ref.26; [e]Ref.25; [f]Ref.49; [g]Ref.65; [h]Ref.6; [i]Ref.90; [j]Ref.26; [k]Ref.78; [l]Ref.80; [m]Ref.110

Table III Predicted values of EAM potentials compared with experimental properties, where the numbers in parentheses represent the experimental data. E_c (eV) is the cohesive energy corresponding to the equilibrium lattice constant a_e (Å) at 300K. Also listed are the equilibrium lattice constants a_e at 0K. a_0 is the lattice parameter corresponding the minimum of the cohesive energy. ε is the linear thermal expansion coefficient (10^{-6} K^{-1}) at 300 K derived from either the QHA method or MD as indicated. Experimental data for thermal expansion coefficients are from Ref. [49].

	E_c	a_e (300K)	a_e(0K)	a_0	ε (MD)	ε (QHA)
Al	-3.36	4.050	4.032 (4.032)[a]	4.018		23.0 (23.2)
Ni	-4.45	3.520	3.511	3.504		13.5 (12.7)
Cu	-3.54	3.615	3.603 (3.603)[b]	3.596		16.8 (16.8)
Rh	-5.75	3.8034	3.797	3.793		7.9 (8.2)
Pd	-3.91	3.890	3.880 (3.879)[c]	3.877		11.2 (11.1)
Ag	-2.85	4.090	4.071 (4.070)[d]	4.064		19.7 (19.1)
Ir	-6.94	3.839	3.835	3.833	6.5 (6.4)	4.8 (6.4)
Pt	-5.77	3.920	3.912	3.909		9.2 (9.2)
Au	-3.93	4.078	4.066 (4.065)[e]	4.061		14.8 (14.2)
Ca	-1.84	5.588	5.570	5.562	20.4 (22.3)	
Sr	-1.72	6.085	6.0712	6.073	17.0 (22.5)	
Pb	-2.85	4.9508	4.928	4.925	28.5 (29.2)	
Ce	-4.32	5.161	5.141	5.132	10.2 (5.2)	
Yb	-1.6	5.485	5.445	5.436	13.2 (25.1)	

[a]Ref. 45; [b]Ref. 46; [c]Ref. 47; [d]Ref. 48; [e]Ref. 49

Table IV Calculated phonon frequencies (THz) at selected symmetry points. The numbers in the parentheses are experimental data. a_0 (Å) is the lattice parameter used for the phonon calculation, and the value underneath it shows the temperature at which the experimental data were taken.

	a_0	$\nu_L(X)$	$\nu_T(X)$	$\nu_L(L)$	$\nu_T(L)$	$\nu_L(K)$	$\nu_{T1}(K)$	$\nu_{T2}(K)$
Al	4.032	9.62	5.80	9.73	4.17	7.68	5.55	8.63
	(80 K[a])	(9.69)	(5.80)	(9.69)	(4.19)	(7.59)	(5.64)	(8.65)
Ni	3.520	8.64	6.42	8.77	4.41	7.98	5.95	7.13
	(300K[b])	(8.55)	(6.27)	(8.88)	(4.24)	(7.73)	(5.78)	(7.30)
Cu	3.603	7.35	5.18	7.40	3.38	5.98	4.68	6.78
	(80K[c])	(7.38)	(5.16)	(7.44)	(3.41)	---	---	---
Rh	3.803	7.01	5.55	7.57	4.66	5.88	5.23	6.23
	(300K[d])	(7.02)	(5.56)	(7.42)	(4.21)	(5.94)	(5.30)	(6.33)
Pd	3.89	6.70	4.48	6.78	3.00	5.26	4.04	6.02
	(300K[e])	(6.71)	(4.58)	(6.84)	(3.20)	(5.33)	(4.10)	(6.03)
Ag	4.090	5.07	3.31	5.04	2.06	4.01	2.96	4.66
	(300K[f])	(5.08)	(3.34)	(4.92)	(2.23)	(3.70)	(3.04)	(4.49)
Ir	3.839	5.72	4.62	3.75	5.95	5.25	4.23	4.72
	(300K[g])	(5.86)	(4.40)	(3.51)	(6.13)	---	(4.16)	(4.78)
Pt	3.910	3.67	5.54	2.45	5.56	4.25	3.16	4.94
	(90K[h])	(3.84)	(5.80)	(2.90)	(5.85)	(4.30)	(3.42)	(5.12)
Au	4.078	4.45	2.75	4.46	1.67	3.60	2.50	4.09
	(300K[i])	(4.61)	(2.75)	(4.70)	(1.86)	(3.34)	(2.43)	(4.03)
Ca	5.588	4.59	3.52	4.46	2.32	3.87	3.11	4.27
	(300K[j])	(4.52)	(3.63)	(4.61)	(2.36)	(3.94)	(3.08)	(4.45)
Sr	6.085	2.46	3.19	1.42	3.03	2.46	2.07	2.97
	(300K[k])	(2.48)	(3.17)	(1.74)	(3.08)	(2.57)	(2.21)	(2.93)
Pb	4.936	2.07	1.55	1.98	0.95	1.66	1.35	1.91
	(80K[l])	(1.86)	(0.89)	(2.19)	(0.89)	(1.75)	(1.25)	(2.02)
Ce	5.162	2.01	3.12	1.28	3.09	2.56	1.85	2.87
	(295K[m])	(2.05)	(3.04)	(0.75)	(2.75)	(2.17)	(1.71)	(2.71)
Yb	5.485	1.79	2.44	1.10	2.39	1.92	1.54	2.25
	(300K[n])	(1.85)	(2.40)	(1.16)	(2.30)	(1.98)	(1.63)	(2.25)

[a]Ref.50; [b]Ref. 51; [c]Ref. 52; [d]Ref. 53; [e]Ref. 54; [f]Ref. 55, [g]Ref. 56, [h]Ref. 57; [i]Ref. 42; [j]Ref. 58; [k]Ref. 59; [l]Ref. 60; [m]Ref. 61; [n]Ref. 62;

Table V Calculated elastic constants C_{11}, C_{12}, C_{14} (GPa) at designated temperatures. The numbers in the parentheses are experimental data at different temperatures taken from Ref. [65,70-73], unless indicated otherwise. K, Y, G indicate the bulk modulus, Young's modulus, and shear modulus in units of GPa, and ν is Poisson's ratio.

	a_0	C_{11}	C_{12}	C_{44}	K	Y	G	ν
Al	4.032	113	61.6	32	77	69	28	0.36
	(0K)	(114)	(61.9)	(31.6)	(76)	(70)	(26)	(0.35)
Ni	3.511	263	154	127	186	217	84	0.30
	(0K)	(261)	(151)	(132)	(180)	(200)	(76)	(0.31)
Cu	3.603	175	124	79	141	125	46	0.35
	(0K)	(176)	(125)	(82)	(140)	(110-128)	(48)	(0.34)
Rh	3.797	420	191	189	267	369	145	0.27
	(0K)	(422)	(192)	(194)	(269)	(319-378 [a])	(150)	(0.26)
Pd	3.880	235	180	82	188	127	46	0.39
	(0K)	(234)	(176)	(71.2)[b]	(180)	(121)	(44)	(0.39)
Ag	4.065	131	97	51	98	78	29	0.37
	(0K)	(132)	(97)	(51)	(100)	(83)	(30)	(0.37)
Ir	3.839	578	241	243	350	525	210	0.25
	(300K)	(582)	(241)	(262)	(320)	(528)	(210)	(0.26)
Pt	3.92	347	253	78	282	180	65	0.39
	(300K)	(347)	(251)	(77)	(228~275[c])	(173[c],168)	(61)	(0.38)
Au	4.078	197	165	45	178	78	28	0.42
	(300K)	(193)	(163)	(42)	(180.3)	(78)	(27)	(0.44)
Ca	5.588	28	18	17	21	26	10	0.30
	(300K)	(28[d])	(18.2[d])	(16.3[d])	(14.1-19.3[e])	(20)	(7.4)	(0.31)
Sr	6.085	16	11	17	12	17	7.1	0.27
	(293K)	(15[f])	(10[f])	(10[f])	(11.5[g])	---	(6.1)	(0.28)
Pb	4.9508	50.1	42.0	15.2	45	25	7.8	0.45
	(300K)	(49.4)	(42.1)	(14.9)	(46)	(16)	(5.6)	(0.44)
Ce	5.161	24.8	13.2	14.6	17.1	25.3	10.2	0.25
	(300K)	(24.1[h])	(10.2[h])	(19.5[h])	(14.8[h], 22)	(34)	(14)	(0.24)
Yb	5.485	21.0	8.34	20.7	13	28	12.7	0.18
	(300K)	(18.6[i])	(10.4[i])	(17.4[i])	(13.1[i])	(24)	(9.9)	(0.21)

[a]A Ref. 74; [b]Ref. 75 (low temperature anomaly); [c]Ref. 76; [d]Ref. 58; [e]Ref. 77; [f]Ref.59; [g]Ref. 78; [h]Ref. 61; [i]Ref. 62

Table VI Calculated structural energy differences, relative to fcc. The numbers in the parentheses are experimental data taken from Ref. [80] unless indicated.

	$\Delta E_{fcc\text{-}hcp}$	$\Delta E_{fcc\text{-}bcc}$	$\Delta E_{fcc\text{-}9R}$	$\Delta E_{fcc\text{-}sc}$	$\Delta E_{fcc\text{-}dc}$
Al	0.03 (0.03)	0.10 (0.12)	0.02	0.27	0.70
Ni	0.024 (0.03)	0.092 (0.12)	0.01	0.60	1.27
Cu	0.01 (0.006)	0.04 (0.04)	0.006	0.44	1.01
Rh	0.01	0.29	0.007	0.69	1.28
Pd	0.026 (0.02)	0.08 (0.11)	0.011	0.52	1.27
Ag	0.006 (0.005)	0.038 (0.04)	0.004	0.41	0.95
Ir	0.07 (0.07)	0.46	0.05	0.79	1.46
Pt	0.03 (0.03)	0.16 (0.16)	0.03	0.39	1.16
Au	0.007 (0.003)	0.004 (0.004)	0.005	0.43	0.95
Ca	0.003 (-0.004~0.012[a])	0.009 (0.013~0.024[a])	0.003	0.395	1.05
Sr	0.007 (0.007[b])	0.006 (0.011[b])	0.005	0.34	1.01
Pb	0.007 (0.003)	0.04 (0.04)	0.005	0.32	0.83
Ce	0.009	0.10	0.007	0.49	1.46
Yb	0.003	0.006	0.006	0.44	0.88

[a]Ref. 81; [b]Ref. 82

Table VII Predicted point defect properties for the fcc metals. Values listed are the relaxed vacancy formation energy E_f^v (eV), migration energy of vacancy diffusion E_m^v (eV), relaxed octahedral and tetrahedral interstitial formation energy E_f^i (Oh) and E_f^i (Td) (eV), and relaxed formation energy of dumbbell defects E_f^d with different configurations. The numbers in the parentheses are experimental values.

	E_f^v	E_m^v	E_f^i (Oh)	E_f^i (Td)	E_f^d [111]	E_f^d [110]	E_f^d [100]
Al	0.67 (0.68 [a])	0.65 (0.65 [b])	2.38	2.85	2.78	2.47	2.21
Ni	1.12 (1.60 [c])	1.02 (1.30 [c])	4.48	4.90	4.79	4.52	4.11
Cu	0.99 (1.03~1.30 [b])	0.74 (0.65[b])	3.17 (2.8-4.2 [c])	3.48	3.43	3.25	2.99
Rh	1.57 (1.71 [d])	1.12	6.4	7.9	7.67	6.78	6.36
Pd	1.44 (1.40 [e])	0.90	4.26	4.87	4.75	4.55	4.23
Ag	1.17 (1.09-1.19[f])	0.65 (0.66[g])	3.35	3.64	3.62	3.48	3.18
Ir	1.67 (1.79 [h])	1.52	10.3	11.9	11.4	10.6	9.39
Pt	1.50 (1.5[b])	0.87 (1.43[e])	4.99	6.38	6.13	5.40	5.11
Au	0.98 (0.89-1.00 [i])	0.79 (0.78-0.88 [j])	3.77	4.31	4.33	4.14	3.89
Ca	0.95 (1.12 [k])	0.60 (0.46 [k])	2.06	1.88	1.95	1.93	1.88
Sr	0.97 (---)	0.56 [---]	2.03	1.91	1.86	1.95	1.84
Pb	0.45 (0.58 [l])	0.48	2.26	2.53	2.40	2.54	2.15
Ce	0.75	0.62	3.30	3.32	3.19	3.10	2.95
Yb	1.42	0.66	1.78	1.79	1.67	1.89	1.89

[a]Ref. 85; [b]Ref. 86; [c]Ref. 87; [d]Ref. 88; [e]Ref. 6; [f]Ref. 91, [g]Ref. 92; [h]Ref.89; [i]Ref.90; [j]Ref.84; [k]Ref.81; [l]Ref.25

Table VIII Calculated surface energies, relaxed stacking fault energies and twining fault energies employing the present EAM potentials.

	Exp.	γ(110)	γ(100)	γ(111)	γ_{SF}	γ_{US}	γ_{T}
Al	980[a]	933	855	634	117(120-144)[g,h]	158	62(75)[i]
Ni	2280[b]	2359	2212	2059	103(125[j])	355	52(43[j])
Cu	1790[b]	1607	1504	1387	53(45[k])	190	27(24[i])
Rh	2659[b]	2381	2481	2233	141(137[l])	693	81
Pd	2000[d]	1747	1645	1529	98(100[m])	232	49
Ag	1140[c]	1125	1042	977	26(22[n])	114	13
Ir	---	2965	2898	2506	317(365[o])	1080	158 (217[p])
Pt	2490[d]	1934	1778	1694	121(110[m])	320	61
Au	1506[d]	1321	1261	1194	30(32[q])	60	15
Ca	490 [e]	477	426	377	8.0	51	4.1
Sr	430[e]	433	374	316	10	36	5
Pb	534[f]	532	476	405	12 (9[n])	81	7.4
Ce	---	797	697	586	21	98	12
Yb	500[e]	527	491	248	19	57	10

[a]Ref. 93; [b]Ref. 94; [c]Ref. 91; [d]Ref. 6; [e]Ref. 95; [f]Ref. 96; [g]Ref. 97; [h]Ref. 98; [i]Ref.93; [j]Ref.86; [k]Ref.99; [l]Ref.100; [m]Ref.101; [n]Ref.25; [o]Ref.102; [p]Ref.103; [q]Ref.26; [n]Ref. 25

Table IX Calculated liquid properties of the fcc metals. T_m (K) denotes the melting temperature (computational error: ± 15 K) ; ΔH_m (kJ/mol) is the melting enthalpy; $\Delta V_m / V_c$ is the volume change upon melting; ρ_m^l (g/cm^3) is the liquid density at the melting temperature; D_m^E and D_m^{GK} (10^{-9} m^2/s) are self-diffusion coefficients calculated using the Einstein method and the Green-Kubo method, respectively. The numbers in the parentheses are experimental data. Experimental data on melting temperature, melting enthalpy and liquid density are taken from Ref. [78,110,111] unless indicated.

	T_m	ΔH_m	$\Delta V_m / V_c$	ρ_m^l	D_m^E	D_m^{GK}
Al	880	8.2	0.044	2.39	6.30	7.12
	(933)	(10.7)	(0.060)	(2.38, 2.37~2.40[a])	(6.30[b])	
Ni	1650	16.1	0.056	7.78	5.20	5.98
	(1728)	(17.5)	(0.045, 0.051)	(7.81)	(4.60[c])	
Cu	1320	11.6	0.057	7.89	3.88	4.94
	(1357)	(13.3)	(0.049, 0.042)	(7.9[k])	(3.96[b])	
Rh	2065	19.30	0.050	10.85	5.67	6.66
	(2237)	(26.59)		(10.82[l])		
Pd	1827	13.9	0.049	10.38	4.38	5.37
	(1828)	(16.74)		(10.38, 10.5[e])	(4.36[d])	
Ag	1255	11.7	0.053	9.37	2.31	3.40
	(1235)	(11.28)	(0.038)	(9.32)	(2.60[b])	
Ir	2280	32.2	0.081	19.0	4.90	5.74
	(2739)	(41.12)		(19.0[j])		
Pt	1890	13.5	0.037	(19.0)	3.63	4.56
	(2041)	(22.17)		(19.2[h])		
Au	1320	11.1	0.049	17.35	1.84	2.81
	(1337)	(12.55)	(0.051)	(17.31, 17.32[f])		
Ca	980	7.56	0.029	1.415	4.60	5.78
	(1115)	(8.54)		(1.378[i])		
Sr	1015	8.77	0.057	2.32	6.89	7.78
	(1050)	(7.43)		(2.32[i])		
Pb	620	5.25	0.041	10.55	1.09	2.36
	(600)	(4.77)	(0.035)	(10.63, 10.64[g])	(2.19[b])	
Ce	1080	11.39	0.015	6.52	5.22	6.32
	(1068)	(5.46)		(6.55)		
Yb	1081			6.34	2.13	3.12
	(1097)	(7.66)		(6.21)		

[a]Ref.112; [b]Ref. 113; [c]Ref.114 theoretical prediction; [d]Ref.115 simulation; [e]Ref. 116; [f]Ref.117; [g]Ref.118; [h]Ref. 119; [i]Ref. 120; [j]Ref. 121; [k]Ref. 122; [l]Ref.123

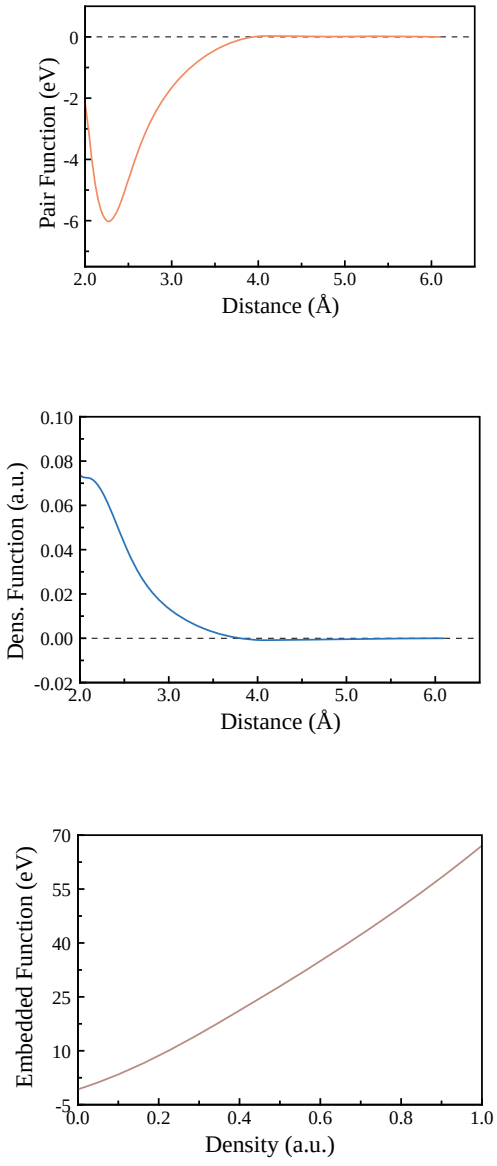

Figure 1 EAM potential plots for Au. The three plots show the slowly varying profiles of the pair function $\phi(r)$, density function $\rho(r)$ and the embedding function $F(n_i)$, respectively, in Eq (1).

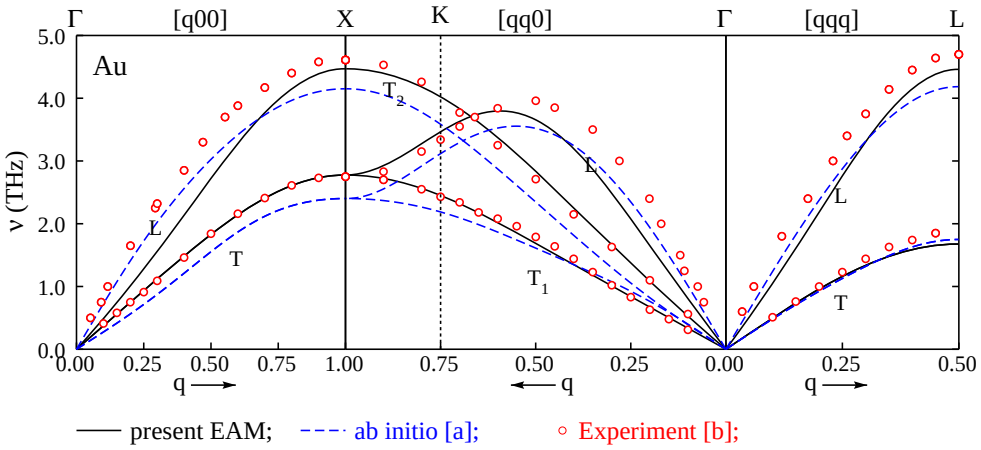

Figure 2 Comparison of phonon-dispersion curves of Au predicted by the present EAM potential model with the experimental values measured by neutron diffraction at 80 K. The phonon frequencies at point *X* were included in the potential fit. Also shown is the *ab initio* calculation using PWSCF.[43] ([a]Ref. 42 and [b]Ref. 43).

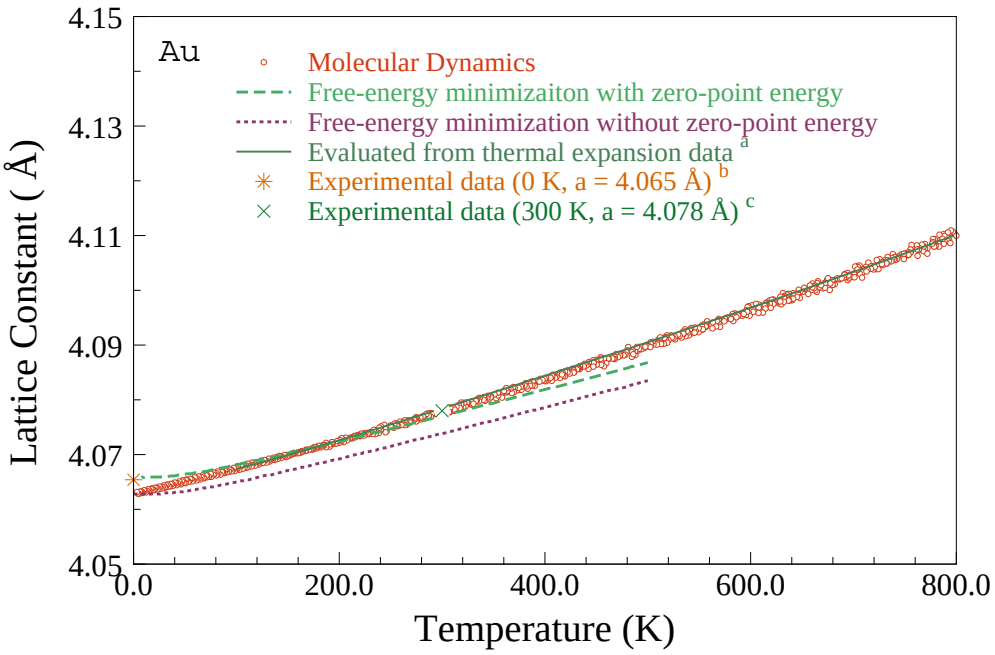

Figure 3 Lattice constant of Au as a function of temperature predicted using the present EAM model. Both the QHA and MD methods were used for the evaluation of the equilibrium lattice constants at different temperatures. The importance of the quantum effect is also shown in the plot by excluding the zero point energy in Eq. (4) in obtaining the lattice constant (see text).

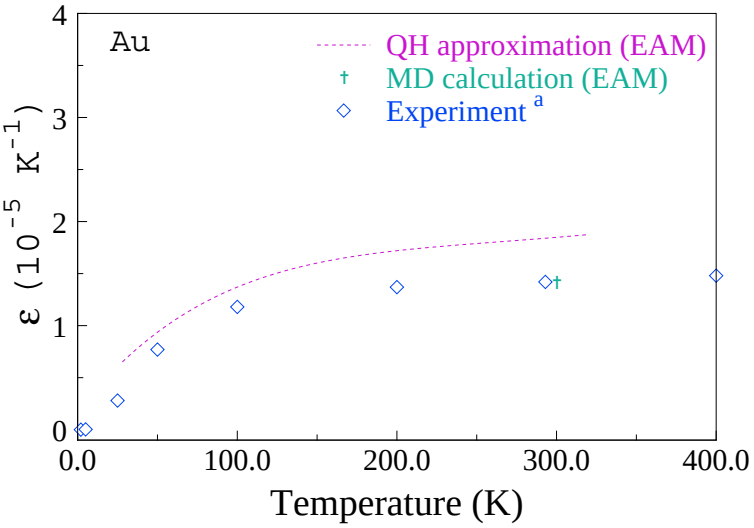

Figure 4 Linear thermal expansion coefficient of Au as a function of temperature.

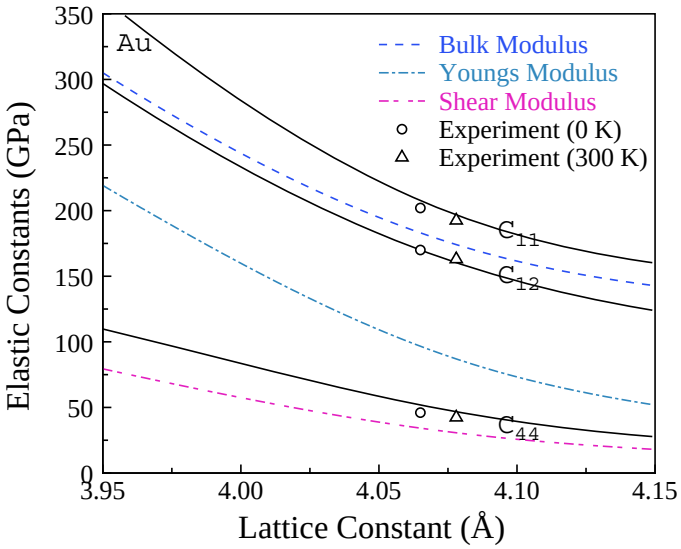

Figure 5 Adiabatic elastic constants of Au as a function of lattice constants (solid black lines), as predicted by the EAM. Also plotted are other important elastic moduli. Experimental elastic constants at room temperature and 0K are shown for comparison.

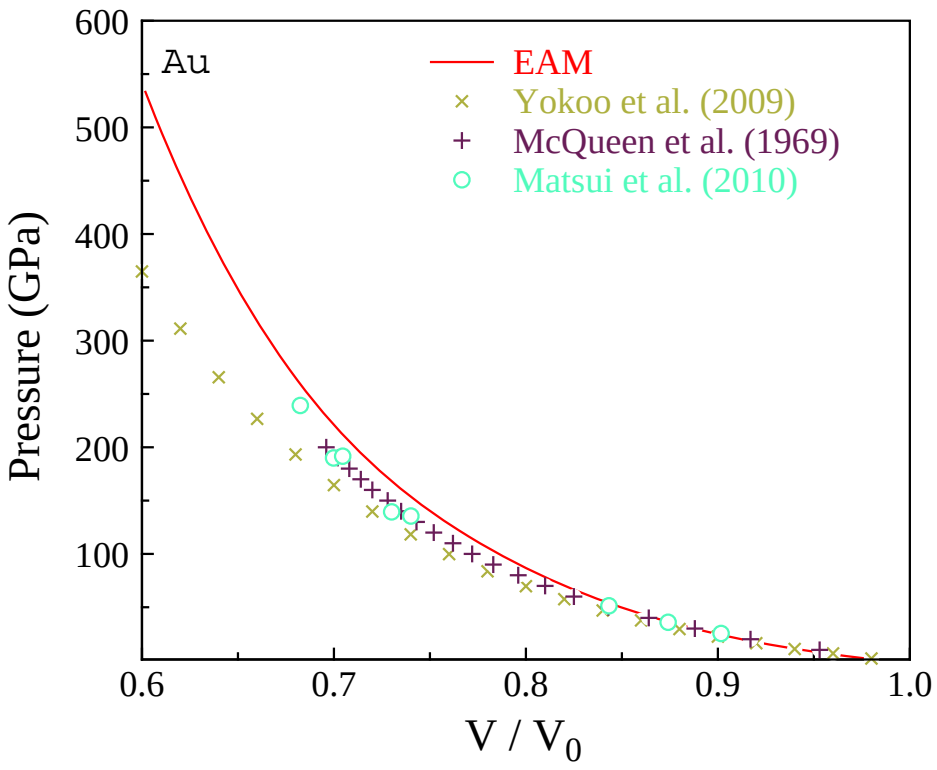

Figure 6 Pressure-volume EOS of Au at T=0 calculated using the EAM model in comparison with experimental data[67-68].

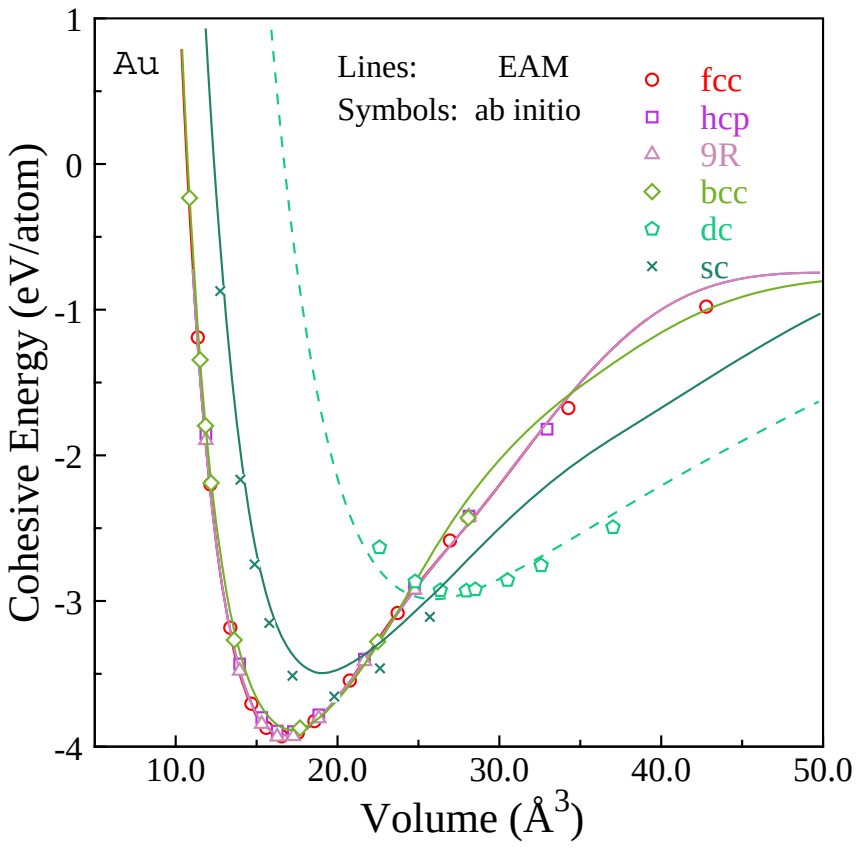

Figure 7 Comparison of *ab initio* and EAM calculations of the cohesive energies of six different crystal structures of Au at different volumes.

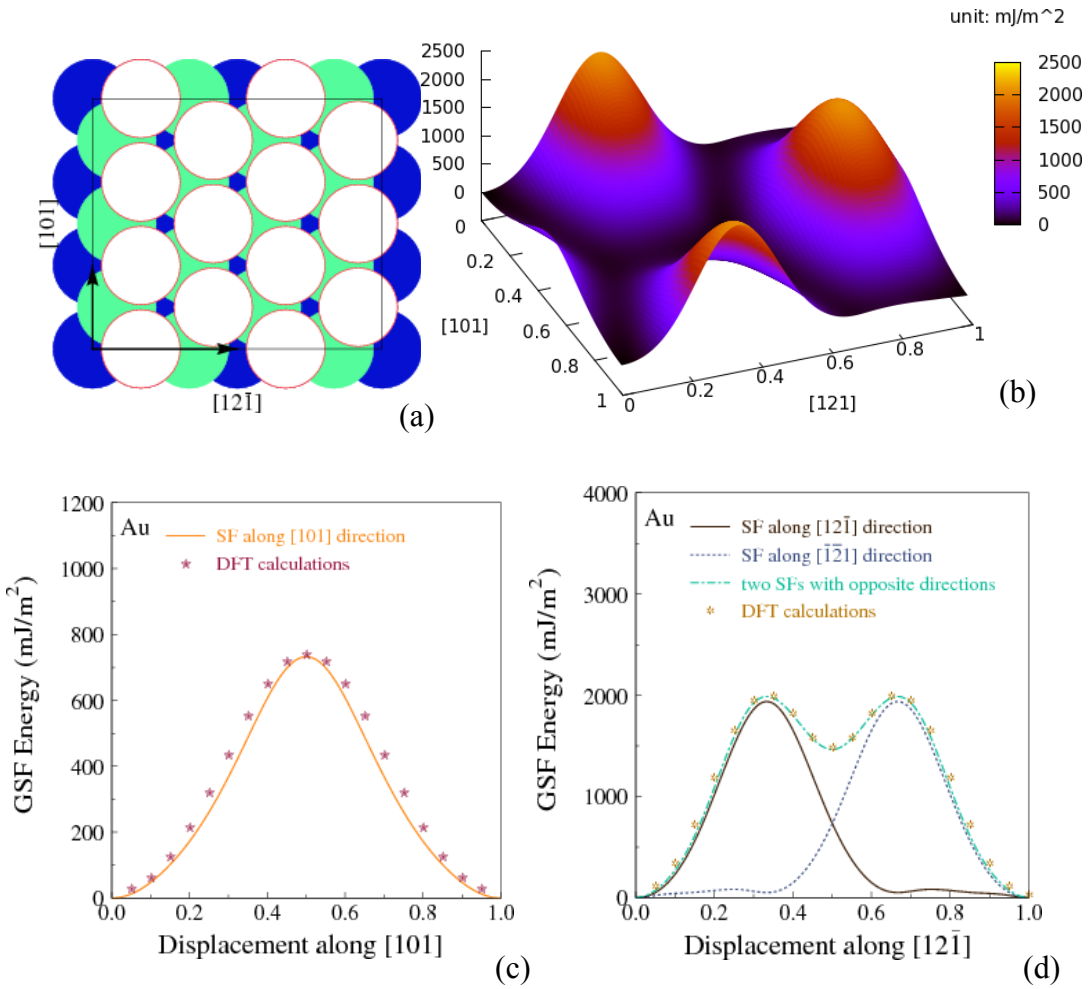

Figure 8 EAM calculations of the γ surface of Au on the (111) plane. (a) Schematic drawing showing the displacements of the (111) plane to obtain the γ surface; (b) EAM calculation of the γ surface; (c) Comparison of the EAM and *ab initio* calculations of GSF energy displaced along the $[0\,\bar{1}\,0]$ direction (unit: $\frac{\sqrt{2}}{2}a$); Comparison of the EAM and ab initio calculations of GSF energy displaced along the $[12\,\bar{1}]$ direction (unit: $\frac{\sqrt{6}}{2}a$) (see text).

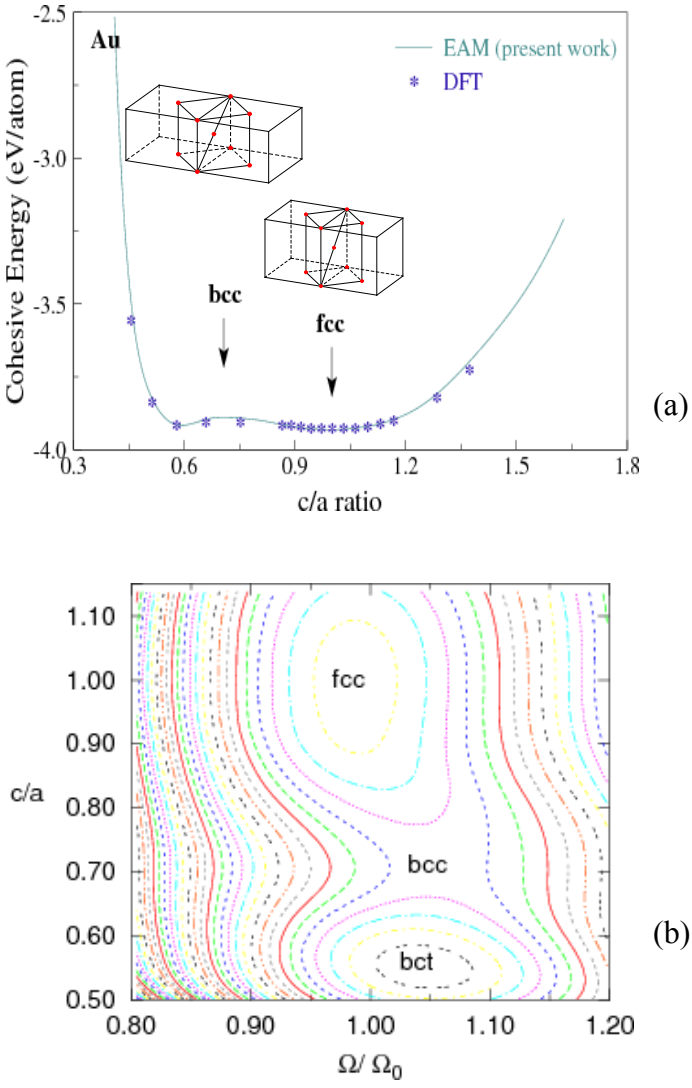

Figure 9 (a) Comparison of EAM and *ab initio* calculations of energy along the tetragonal Bain path between fcc and bcc structures. Calculations were performed at a constant volume corresponding to the equilibrium fcc phase. (b) Contour plot of the PES for centered tetragonal Au as a function of c/a and the reduced volume Ω/Ω_0. The contour spacing is 5 meV.

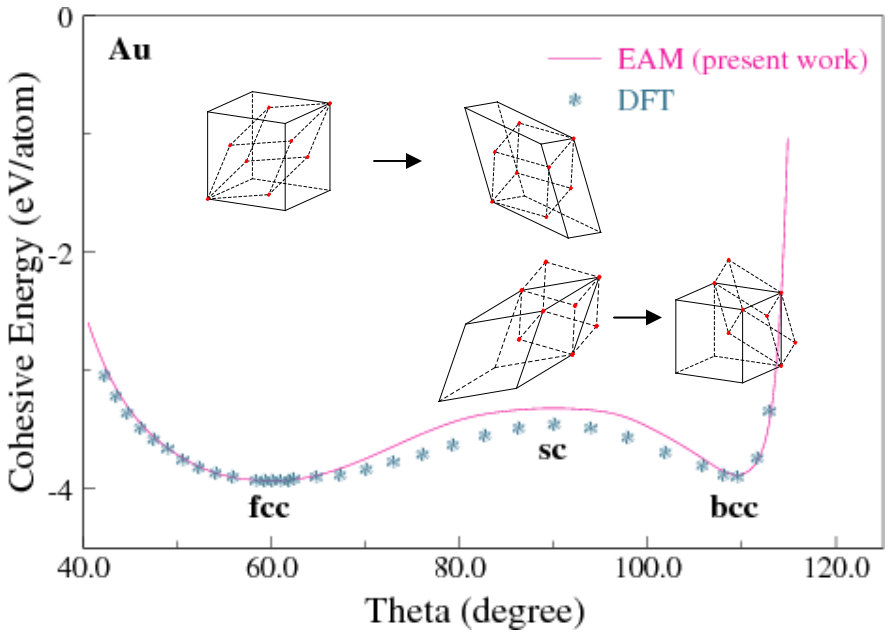

Figure 10 Comparison of EAM and *ab initio* calculations of energy along the trigonal Bain path between fcc, sc and bcc structures. Calculations were performed at a constant volume corresponding to the equilibrium fcc phase. The draws in the inset shows the structural deformation along the trigonal deformation path.

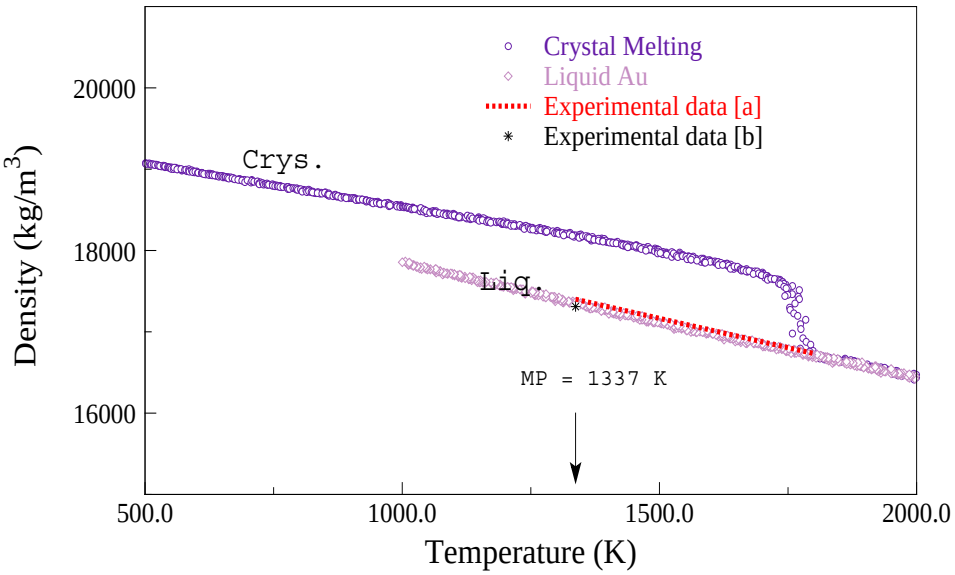

Figure 11 Density changes of Au during melting and freezing, as obtained from NPT molecular dynamics simulations (32,000 atoms) employing the present EAM potential. ([a]Ref. 117, [b]Ref.111)

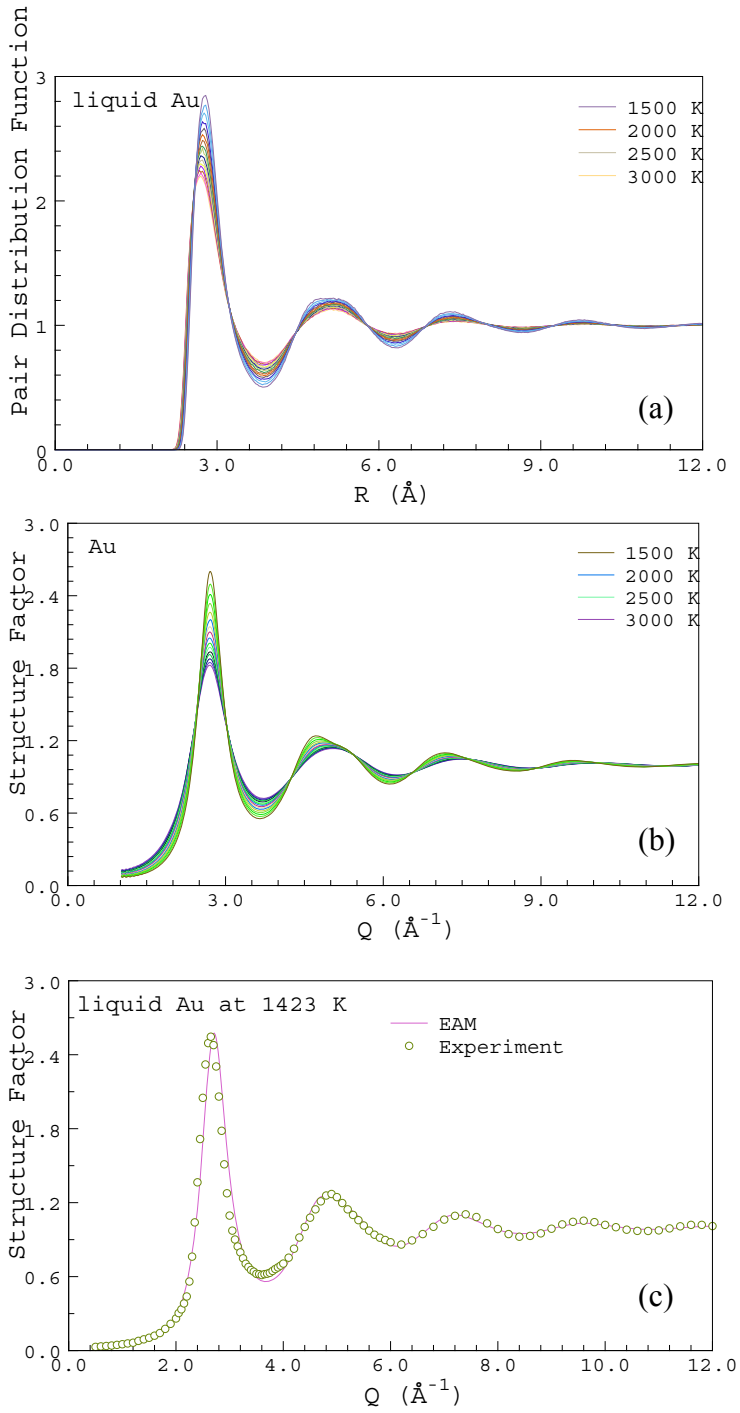

Figure 12 (a) The evolution of RDF of liquid Au at different temperatures employing the EAM potential; (b) Structure factor $S(Q)$ of Au as a function of temperature; (c) Comparison of experimental [126] and theoretical $S(Q)$ of liquid Au near the melting point.

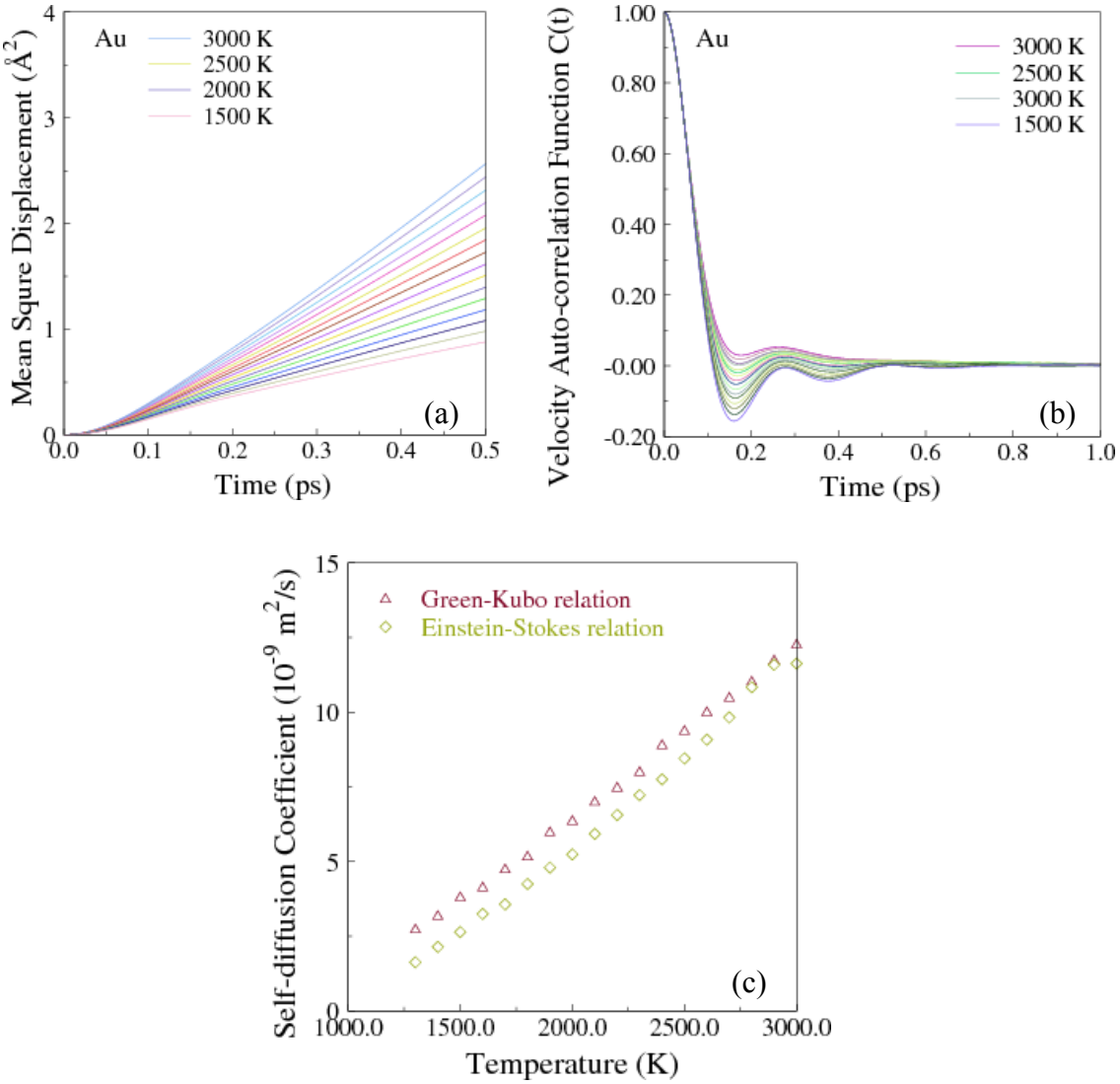

Figure 13 (a) MSD of liquid Au during molecular dynamics equilibration at different temperatures. (b) Velocity auto-correlation functions of liquid Au at different temperatures. (c) Self-diffusion coefficient of Au at different temperatures, as derived from the Einstein and the Green-Kubo methods.

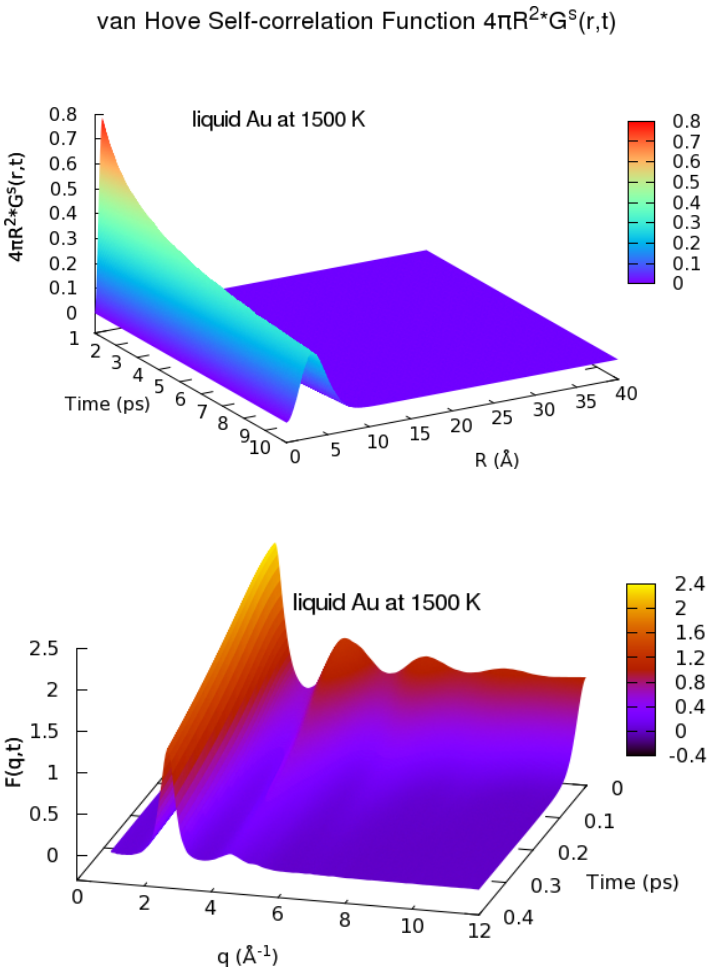

Figure 14 Dynamical properties of Au examined by means of (a) the van Hove self auto-correlation function; (b) self-intermediate scattering function of Au. Both plots were plotted against time to show their dynamical evolution (see text).